

IMAGE PROCESSING OF TRIPLE SHOCK
WAVE EVOLUTION

By

KATHERINE MICHELLE YARBROUGH

Presented to the Faculty of the Graduate School of
The University of Texas at Arlington in Partial Fulfillment
of the Requirements for the degree of

MASTERS OF SCIENCE IN AEROSPACE ENGINEERING

THE UNIVERSITY OF TEXAS AT ARLINGTON

May 2016

Supervising Committee:

Frank K. Lu (Supervising Professor)
Donald R. Wilson
Zhen X. Han

Copyright © by KATHERINE MICHELLE YARBROUGH 2016

All Rights Reserved

Acknowledgements

I would like to thank Dr. Frank Lu for guiding me through my research and aiding in my thesis preparation while at The University of Texas at Arlington. Having Dr. Lu as a supervisor was enormously educational in furthering my horizons through research. I am very grateful to have had the opportunity to be a research assistant at the Aerodynamics Research Center and working on funded projects with Dr. Dibesh Joshi and Dr. Frank Lu, I learned so much during my short time at the ARC. Working on pulsed detonation engines was easily some of the most memorable experiences at UT Arlington. I would like to express my gratitude to my thesis committee members, Dr. Wilson and Dr. Han, for their comments and critiques about my work. I am grateful for their time and commitment to furthering my thesis. I am very appreciative to Dr. Dibesh Joshi, James Peace, and Raheem Bello for helping with the set up and capturing of the images needed for this work. Working with you helped me learn about pulsed detonation engines and high speed photography, thank you. David Carter provided advice and help while I was at the ARC, which I am very grateful for as well.

Lastly, I would like to thank my friends, family, and specifically Gretchen who supported and encouraged me during my graduate school education. Without your help my sanity would have been gone years ago.

March, 28, 2016

Abstract

IMAGE PROCESSING OF WAVE EVOLUTION OF TRIPLE SHOCK INTERSECTION

Katherine Yarbrough, M.S

The University of Texas at Arlington, 2016

Supervising Professor: Frank K. Lu

Shock diamonds occur in over- or under- expanded supersonic flow. They occur in the unsteady jet of a pulse detonation engine, displaying an array of complex features. Due to the highly transient nature of the flow, it must be captured using high-speed cinematography. A study of image processing of shock reflection in unsteady flow is presented. Using a computer-based environment, a method was developed to process images of shock waves to pinpoint where the shock wave starts. Using mathematical methods, such as Abel transforms, a computer code, written in Matlab, was developed to accurately transform the images to detect density distributions in the form of shock waves. The Mach number and specific heat, pressure, temperature, and density ratios were found using shock polars. Evolution of the flow was examined by transforming images to follow the flow patterns. Seven images were selected and analyzed with the methods developed in this thesis. Then a comparison was done by tracking particles seeded in the flow. The particle tracking revealed velocities which were compared to the Mach numbers found using the shock polars.

Table of Contents

Acknowledgements	4
Abstract	5
Table of Contents	6
List of Figures	8
List of Tables	10
Chapter 1: Introduction	11
Chapter 2: Image Processing	14
2.1 Set Up	14
2.2 Inverse Abel Transform	16
2.3 Hodograph	26
Chapter 3: Evolution of Flow	34
3.1 Image 1	36
3.2 Image 2	38
3.3 Image 3	39
3.4 Image 4	42
3.5 Image 5	45

3.6 Image 6.....	48
3.7 Image 7.....	51
3.8 Velocity Calculations	55
Chapter 4: Conclusion.....	60
References.....	61
Appendix A: Inverse Able Transform Code	63
Appendix B: Hodograph Code	66
Appendix C: CEA Output	73
Appendix D: Velocity Calculations	77

List of Figures

Figure 1-1: Depiction of Mach reflection	13
Figure 2-1: Image of PDE exhaust.....	15
Figure 2-2: Axis of symmetry	17
Figure 2-3: Cropped image of PDE exhaust	20
Figure 2-4: Lambda foot focus of exhaust	20
Figure 2-5: Transformed image	21
Figure 2-6: Fig. 2-5 on calibration plate	22
Figure 2-7: Annotated Fig. 2-6	23
Figure 2-8: Mach features identified	24
Figure 2-9: Shock polar with initial guess for reflected shock wave	30
Figure 2-10: Shock polar of Image 2	33
Figure 3-1: Flow evolution images	34
Figure 3-2: Image 1 in flow evolution	36
Figure 3-3: Post transform of Fig. 3-2	36
Figure 3-4: Shock polar of Fig. 3-2	38
Figure 3-5: Image 3 in flow evolution	39
Figure 3-6: Post transform Fig. 3-5	39

Figure 3-7: Shock polar of Image 3	41
Figure 3-8: Image 4 in flow evolution	42
Figure 3-9: Post transform Fig. 3-8	43
Figure 3-10: Shock polar of Image 4	44
Figure 3-11: Image 5 of flow evolution	45
Figure 3-12: Post transform Fig. 3-10	46
Figure 3-13: Shock Polar of Image 5	47
Figure 3-14: Image 6 in flow evolution	48
Figure 3-15: Post transform of Fig. 3-14	49
Figure 3-16: Shock polar of Image 6	50
Figure 3-17: Image 7 in flow evolution	51
Figure 3-18: Mach reflection with no triple point	52
Figure 3-19: Post transform of Fig. 3-17	53
Figure 3-20: Shock polar for Image 7	54
Figure 3-21: TiO ₂ nanoparticle identification	55
Figure 3-22: Particle tracking image at 0 ns	56
Figure 3-23: Particle tracking image at 20,000 ns	56

List of Tables

Table 2-1: Percent change for angles	25
Table 2-2: Deflection angles	31
Table 2-3: Percent change for calculated variables	32
Table 3-1: Time stamps for images in flow	35
Table 3-2: Shock polar results of Image1	37
Table 3-3: Shock polar results of Image 3	40
Table 3-4: Shock polar results of Image 4	42
Table 3-5: Shock polar results of Image 5	46
Table 3-6: Shock polar results of Image 6	49
Table 3-7: Shock polar results for Image 7	53
Table 3-8: Length and velocity calculation	57
Table 3-9: Particle velocities	58
Table 3-10: Time for each flow evolution image	59
Table 3-11: Incident and reflected shock wave Mach number	59

Chapter 1: Introduction

A series of shocks and expansions form when an over- or an under-expanded flow leaves a supersonic nozzle [1]. These shocks and expansions appear to be diamond-shaped in Schlieren or shadowgraph images and are thus typically called shock diamonds. Expansion fans occur when the flow is turned away from itself causing the flow to expand, while shock waves form when the flow is turned into itself causing the flow to compress. Once the flow starts expanding, the expansion fan reflects off the free jet boundary as a compression fan [2]. Directly after the region of low pressure flow comes a region of high pressure flow where oblique shock waves form. A ramp can produce an attached oblique shock wave, but if the ramp angle is too large the shock wave will detach from the ramp. Normal shock waves form when a detached shock wave has a wave angle of 90° [1]. The flow alternates between low pressure and high pressure until the flow reaches atmospheric conditions through viscous dissipation. The combined shock loss and viscous dissipation causes the imperfectly expanded jet to completely dissipate.

Likewise, a ramp can produce an attached oblique shock wave. This oblique shock is also known as a weak shock because oblique shock theory yields two solutions [1]. The strong solution has thus far not been observed in experiments. If the ramp angle is too large the shock wave will detach from the ramp. The detached shock, also known as a bow shock, stands off in front of the

wedge and is normal to it [1]. The detached shock curves around and approaches the weak solution in the farfield.

Under some circumstances, a propagating supersonic flow passes a ramp through a “lambda” shock system, whereby a strong normal shock bifurcates into two oblique shocks forming the legs of the lambda-foot system as shown schematically in fig. 1 [3]. This shock formation is sometimes known as Mach reflection. The main, normal shock is also called the Mach stem, or Mach disk. The schematic shows the Mach stem as a straight shock although in reality it is bowed toward the downstream at the triple-shock intersection. The mismatch in entropy between the main shock and the two oblique shocks results in a slip line accompanied by a system of expansions and compressions [3].

The evolution of the triple-shock intersection through an unsteady jet is the emphasis of this thesis. The unsteady jet was established by the blowdown process when a blast wave exits a detonation tube. High speed cinematography was employed to capture images that were subsequently analyzed to gain insight into Mach reflections. A method was developed in a computer-based environment to determine features in the Mach reflection. The method pinpoints the triple-shock interaction with pixel width definition using image processing tools in Matlab. Following the location of the triple-shock interaction and with knowledge of the incoming flow, all downstream conditions through the lambda foot can then be determined.

The blast wave was created by the exit of a detonation wave in a tube. The reflected shock wave Mach number is assumed after the incident shock wave is found using the wedge angle and the incident shock wave angle. The specific heat ratio is found using the NASA Chemical Equilibrium with Applications applet.

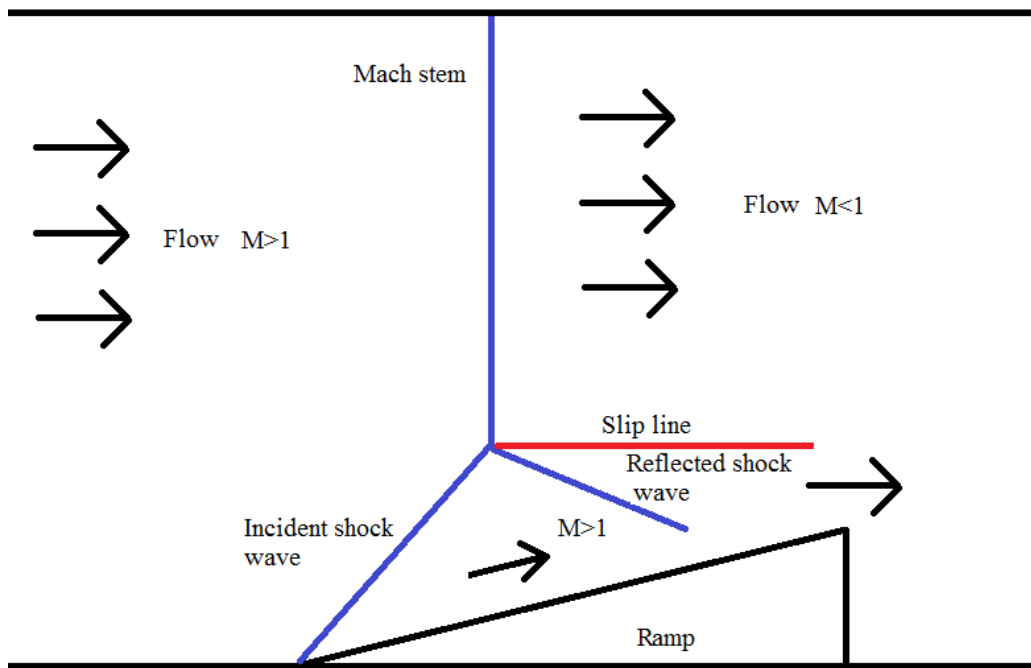


Figure 1-1: Depiction of Mach reflection

Chapter 2: Image Processing

2.1 Set Up

The experiments were performed using a pulsed detonation engine operated to deliver a single detonation. Details of this engine were briefly reported in Lu et al. [4]. A single detonation is adequate for the experiments; the image will not be hindered by noise or reverberation from a previous detonation. The PDE used in the test was fueled by hydrogen and used oxygen for the oxidizer, both in gaseous state. A minute amount of titanium dioxide nanoparticles was coated inside the detonation tube. The flame from the detonation illuminates the nanoparticles, the light of which is captured by a high-speed camera.

A Shimadzu HPV-X high speed camera was arranged to view perpendicularly to the jet and focused with a LaVision Type 20 calibration plate. The pictures were taken with no filter, 50,000 frames per second with a delay between pictures at 20 μ s. For each detonation, the camera captured 256 images. Titanium dioxide (TiO_2) nanoparticles (LaVision 1108953) were seeded in the PDE between detonations, can be seen as specks of white and traced through the flow evolution. This created an informative view of the jet exhaust exiting the PDE. An example picture is given in Fig. 2-1.

In Fig. 2-1 the general shapes that are seen in the picture are the end of the PDE tube towards the right of the image, the flow pattern exiting the tube, and the Mach reflection towards the center of the frame.

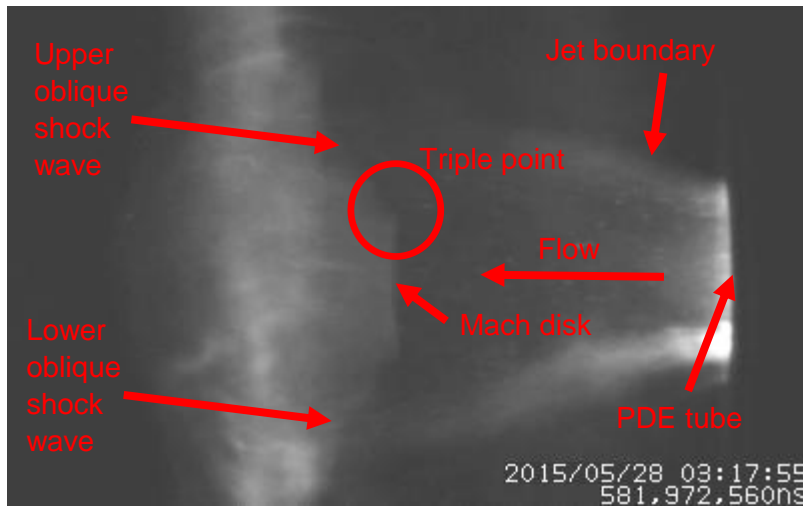


Figure 2-1: Image of PDE exhaust

The Mach stem, or Mach disk is prominent in the center of the flow cylinder, as well as the oblique shock waves reflecting off the Mach stem at angles. Also, the shape of an under expanded flow pattern emerges from the expansion of the gas just after the exit from the tube. Flow exiting the PDE tube expands outward from the radius of the tube which is explicit of under-expanded flow.

The images selected for transformation all had similar qualities to Fig. 2-1, such as a clear view of the Mach reflection with views of the subsequent lambda foot. Finding images with a clear view of the Mach reflection can prove to be difficult. The development of the Mach reflection happened at the front end of the flow exhaust evolution, so the search for the Mach reflection in the images is made easier with this information. The use of a rudimentary image editing software was utilized to increase the contrast between black and white to provide more clarity to see the shapes in the images.

2.2 Inverse Abel Transform

Once the pictures are taken and selected, computer based algorithms for inverse Abel transforms are developed to process the images for refinement of Mach features [5]. The Abel transform will be described later. The inverse Abel transform allows the image to be processed using density distributions [6]. The pictures are overlaid on a calibration plate photo taken with the same camera settings as in Chapter 2.1 to get a distance measurement so angles can be calculated on the exhaust pictures.

The Abel transform was developed in the early 1800s by Niels Henrik Abel. Abel transforms are an integral transform, similar to Fourier and Laplace transforms, that project some function of an object onto an axis [6]. The projection can only be done if the object in question is axially or spherically symmetric. Typically Abel transforms are used in plasma physics because of the unique analysis of symmetric bodies. However, the Abel transform is applied to the images of the PDE exhaust in this case. The symmetry is about the long side of the image in Fig. 2-2 through the center of the PDE tube.

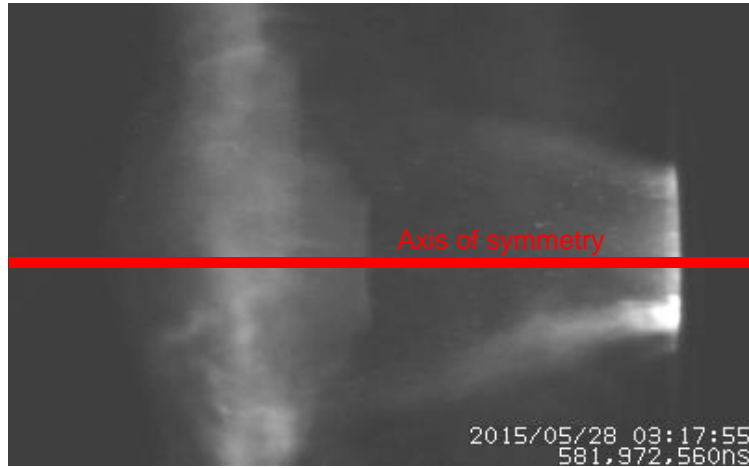


Figure 2-2: Axis of symmetry

The symmetry is one part of the transform, next the equations. The Abel transform is given by the equation,

$$f(x) = 2 \int_x^{\infty} \frac{f(r)r \, dr}{\sqrt{r^2 - x^2}}$$

where the function of the radius, $f(r)$, is an emission function that correlates to the body of the object. The transform takes a function and creates a density distribution onto a plane. For the analysis of the jet exhaust the black and white pictures are mapped with black as the least dense and white at the most dense area of the picture because of the light reflecting from titanium dioxide particles seeded in the detonation engine. The inverse of this transform takes an image and calculates the emission function. To find where the edges of the shock wave are the image must be imported into Matlab and used in the calculation of the inverse transform. The inverse transform is given by the equation,

$$f(r) = -\frac{1}{\pi} \int_r^{\infty} \frac{df}{dx} \frac{dx}{\sqrt{x^2 - r^2}}$$

The inversion of the Abel transformation can be performed using Pretzler's method [7]. The method uses cosine functions as the function of the radius in the Abel transform, then once the cosine functions are calculated the integral is inverted to create the emission function that will be used to generate the transformed image. Below are the cosine functions,

$$f_n(r) = 1 - (-1)^n \cos(n\pi \frac{r}{R})$$

where r is the function to be integrated over, R is the radius of the object, and n is the number of cosine expansions needed for the transform. More cosine expansions introduced into the final transformed image increases the amount of noise considered in the image transformation. Some Mach features may be easier to transform than others, so having the ability to choose the cosine frequency limit makes the code more proficient. This method does not use any derivatives making it a simpler method of inverting the Abel transformation. The final inverse Abel transform is below,

$$f_n(x) = \int_x^R f_n(r) \frac{r}{\sqrt{r^2 - x^2}} dr$$

This inverse Abel transform code can be seen in Appendix A, and the function in the code is now described. The inputs to the inverse Abel transform function are the matrix lines of the image; the cosine frequency limit; and the radius of the system, where the system is the length of the matrix. The cosine frequency limit

adjusts how much noise is in the image. Since the transform is a density distribution, the features that will transform the easiest are the densest, or the areas with the most TiO_2 particles. The Mach features being explored are not the densest regions in the image, so they might not be transformed properly. Therefore, a high upper limit for the cosine expansions is used to define the features better. The image matrix is fed through a loop, line by line, of the inverse Abel function.

Performing a transform with a high cosine frequency limit is time consuming, so another method to define the Mach reflections during the transformation is the selective cropping of the image. The transformation can have a grainy effect for flow that doesn't follow the line of symmetry for the image and Mach features can even be missed altogether, so cropping the image to focus on the Mach features can yield a more enhanced transformation. For smaller or more delicate features, rotating the image to make the flow perpendicular to the long side of the image will also bring out more effective transformations. This rotation is useful when transforming the lambda foot reflecting off the Mach stem. The direction of flow must be going from left to right in the image. For Fig. 2-1 the flow is going from right to left so it must be flipped.

Fig. 2-1 is an example of an original image before transformation, Fig. 2-3 is an image cropped to force the Matlab code to focus on the Mach stem, and Fig. 2-4 is an example of cropping done to focus on the lambda foot. In Fig. 2-3, below, the image was flipped on the vertical axis to align the flow with the direction of

travel of the code. Also, in Fig. 2-3 the Mach stem is the first feature in the image that the code comes to, where in Fig. 2-4 the lambda foot is the first feature.

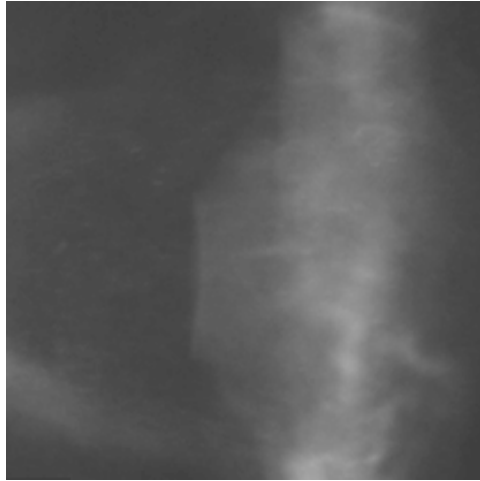


Figure 2-3: Cropped image of PDE exhaust

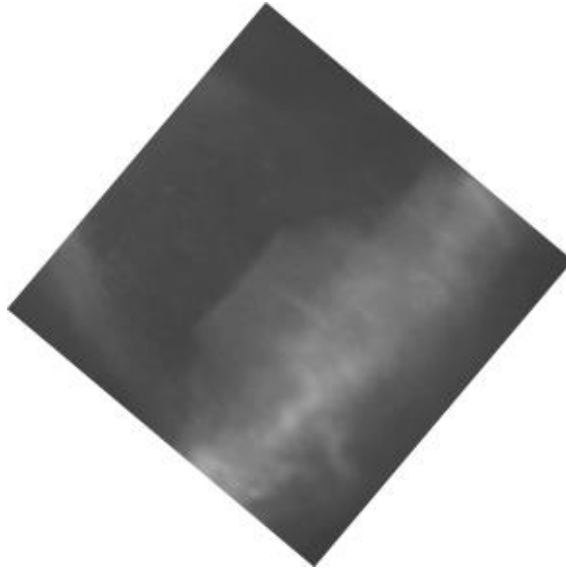


Figure 2-4: Lambda foot focus of exhaust

The code was written to allow for the contrast settings to be binary, namely, pure black and pure white, with no gray. This is done by adjusting the minimum and maximum window for color. This creates a clearer image to determine precisely where the shock wave starts in the image. Below, Fig. 2-5 is a post transformation image of Fig. 2-4. The purpose of this transformation was to highlight the lambda foot oblique shock wave.

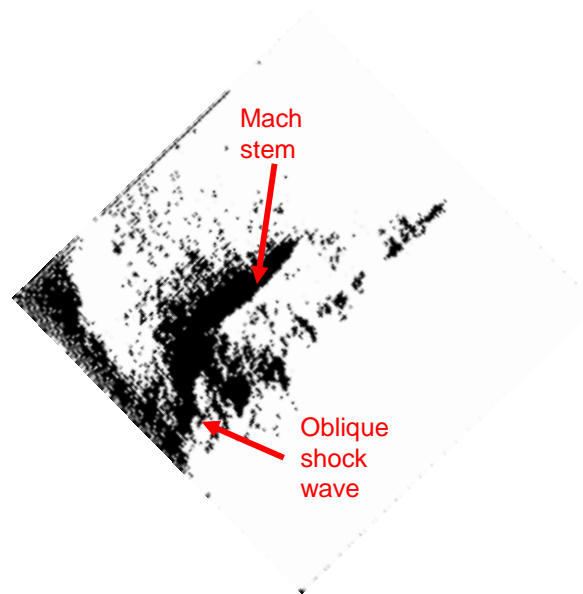


Figure 2-5: Transformed image

Comparing Fig.2-5 to Fig. 2-4, there is a significant difference between the crisp nature of the Mach stem and the lambda foot in Fig. 2-5 and the blurriness in Fig. 2-4. In Fig. 2-3 there is a slight fuzziness to the Mach stem towards the center where in the Fig. 2-5 it is completely gone, revealing only the shock wave. Fig. 2-4 is rotated to focus on the lower lambda foot, so the upper lambda foot is nearly

parallel with the long side of the image, because of this in Fig. 2-5 the upper lambda foot is lost. The best results come from when the desired flow patterns are perpendicular to the long side of the image.

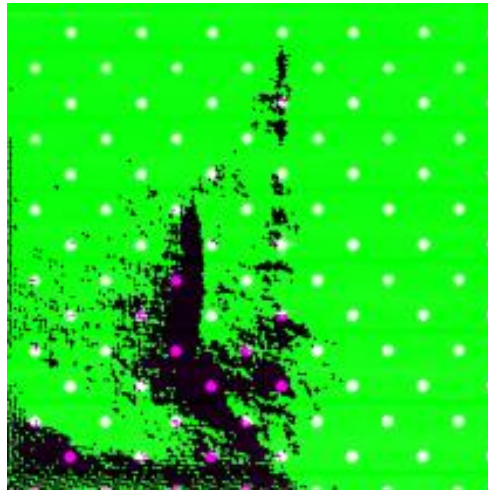


Figure 2-6: Fig. 2-5 on calibration plate

After obtaining the transformed image, the location of the key features of interest was determined through the use of the calibration plate image. The calibration plate image is overlaid on the transformed image. The calibration plate used during the testing is a LaVision Type 20 calibration plate, which puts the distance between dots at 15 mm. A pixel to millimeter equivalence is set at 30 pixels between dots or 2 pixels per millimeter. Below, Fig. 2-6 is Fig. 2-5 overlaid on a calibration plate image. From Fig. 2-6 and 2-7, a zoomed in image of Fig. 2-6, angles and distances can be measured.

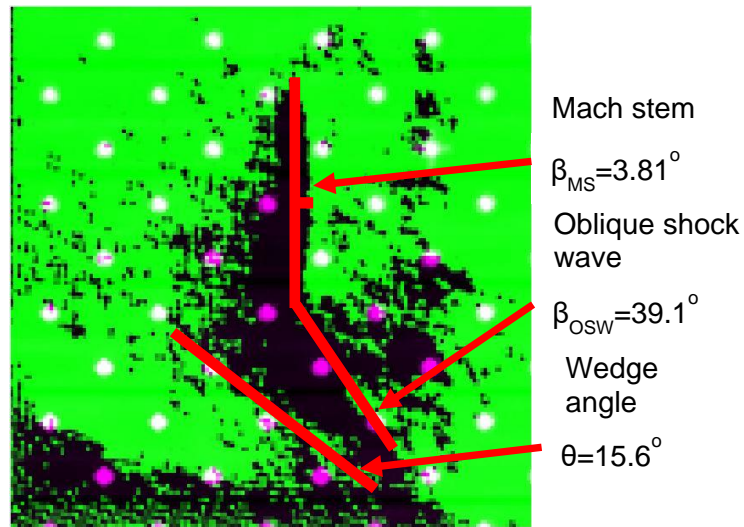


Figure 2-7: Annotated Fig. 2-6

The deflection angle of the under-expanded flow is calculated to be 15.57° , the incident oblique shock wave is measured at 39.09° , and the normal shock wave is measured at 3.81° . Since the normal shock wave has an angle larger than zero it is technically an oblique shock wave, this can be seen in Fig. 2-7 where the oblique shock wave, or Mach stem, has a slight curve. The flow downstream of the shock waves is separated into two streams, the flow downstream of the Mach stem and the flow downstream of the oblique shock wave because the strengths of the waves are different. The difference in pressure, temperature, etc. between the flow streams means the properties across this line are discontinuous, this line is called a slip line [3]. In order for the flow to turn back to the free stream flow a second shock wave must be present, a reflecting shock wave.

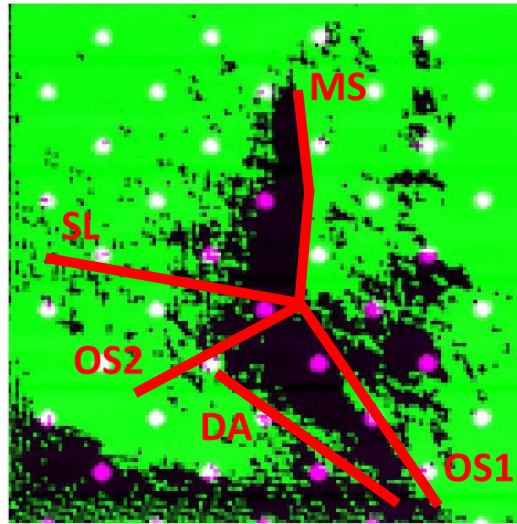


Figure 2-8: Mach features identified

Fig. 2-8 shows where all the features are; DA is the deflection angle of the wedge, MS is Mach stem, OS1 is the incident oblique shock wave, SL is slip line, and OS2 is the reflected oblique shock wave that is assumed from the existence of the slip line.

The percent change for the angle calculations was done by changing 1 pixel coordinate at a time and finding the change, a total of 12 points were analyzed for each angle. From Table 2-1, the wedge angle had the most change between each step while the incident shock wave had the least. The maximum change between each step was 5.6% change for the wedge angle.

Table 2-1: Percent change for angles

Normal shock wave					
x	y	x	y	Angle	Change
206	111	208	143	3.58	
206	112	208	143	3.69	3.2%
206	113	208	143	3.81	3.3%
206	113	208	142	3.95	3.4%
206	113	208	141	4.09	3.6%
206	113	208	140	4.24	3.7%
Incident shock wave					
x	y	x	y	Angle	Change
208	113	240	90	35.7	
208	113	240	89	36.9	3.3%
208	113	240	88	38.0	3.1%
208	113	240	87	39.1	2.9%
208	112	240	87	38.0	-2.8%
208	111	240	87	36.9	-3.0%
Wedge					
x	y	x	y	Angle	Change
100	194	161	213	17.3	
100	195	161	213	16.4	-5.0%
100	196	161	213	15.6	-5.3%
100	196	161	214	16.4	5.6%
100	196	161	215	17.3	5.2%
100	196	161	216	18.2	4.9%

2.3 Shock Polar

A shock polar plot code is developed to make shock polars of the transformed images, see Appendix B. This code was produced using Collar's Theorem, an iterative approach to finding parameters such as shock wave angle, Mach number behind the shock waves and pressure and temperature ratios for flow behind and in front of the Mach stem and the lambda foot [8]. Using the offset angle determined from the pictures and the assumed Mach number and specific heat ratio, a shock polar is formed.

From Fig. 2-6, it is possible to measure the angles of the Mach stem, oblique shock wave, and deflection angle. The upstream Mach number of the lambda foot is calculated using the implicit shock angle equation below [9],

$$\tan \theta = 2 \cot \beta \frac{M_1^2 \sin^2 \beta - 1}{M_1^2 (\gamma + \cos 2\beta) + 2}$$

Using an initial assumption of specific heat ratio 1.4 and the angles found in Chapter 2.2, this equation results in a downstream Mach number of 2.38. In Matlab an if statement equates each side until a loop reaches the preset tolerance level. After the Mach number upstream of the shock wave is calculated the coefficients used in Collar's Method are calculated from the equations below [8],

$$x_{n+1} = + \sqrt{A - \frac{B}{x_n - C}}$$

where n is the number of iterations to be performed, and A, B, and C are given by

$$A = M_1^2 - 1$$

$$B = \frac{1}{2}(\gamma + 1)M_1^4 \tan \theta$$

$$C = \left[\frac{1}{2}(\gamma + 1)M_1^2 + 1 \right] \tan \theta$$

Finally, the first x is approximated using

$$x_1 = \sqrt{M_1^2 - 1}$$

This method was developed by Arthur Roderick Collar, who showed that the implicit equation for the shock angle can be written as a cubic function. When the iteration is performed using a cubic function the weak shock solution is found, using only A, B, and C the weak shock solution is x_0 . Factoring this equation yields a quadratic function, below

$$x^3 + Cx^2 - Ax + (B - AC) = 0$$

$$x^2 + (C + x_0)x + [x_0(C + x_0) - A] = 0$$

which has the solution of

$$x = \frac{1}{2} \left[-(C + x_0) \pm \sqrt{(C + x_0)(C - 3x_0) + 4A} \right]$$

This gives two solutions, positive and negative. The positive solution gives the strong shock solution, where the negative solution is an expansion shock which is impossible. The angle of the shock wave is calculated using three equations, one

equation each for the maximum shock wave angle and the angles for the strong and weak shock solutions; the equations are given below, respectively,

$$\sin^2 \beta_m = \sqrt{\frac{1}{\gamma M_1^2} \left[\frac{\gamma + 1}{4} M_1^2 - 1 + \sqrt{(\gamma + 1) \left(1 + \frac{\gamma - 1}{2} M_1^2 + \frac{\gamma + 1}{16} M_1^4 \right)} \right]}$$

$$\tan \beta = \frac{1}{\frac{1}{2} \left[-(C + x_f) + \sqrt{(C + x_f)(C - 3x_f) + 4A} \right]}$$

$$\beta = 90^\circ - \text{atan}(x_n)$$

where x_f is the coefficient calculated in the final iteration. The maximum deflection angle is calculated next using the maximum shock wave angle, below,

$$\tan \theta_m = \frac{1}{\tan \beta_m \frac{M_n^2 - 1}{\frac{\gamma + 1}{2} M_1^2 - M_n^2 + 1}}$$

where M_n is the Mach number normal to the shock wave. Once the maximum deflection angle is found the rest of the deflection angles are linearly spaced out numbers from 0 to the maximum deflection angle. After the shock wave and deflection angle vectors are formed the pressure, temperature, density, entropy, and downstream Mach number of the Mach stem are calculated [1], [3], [9].

$$\frac{p_2}{p_1} = \frac{2\gamma M_n^2 - (\gamma - 1)}{\gamma + 1}$$

$$\frac{\rho_2}{\rho_1} = \frac{(\gamma + 1) M_n^2}{2 + (\gamma - 1) M_n^2}$$

$$\frac{T_2}{T_1} = \frac{p_2 \rho_1}{p_1 \rho_2}$$

$$\frac{\Delta s}{R} = \frac{\gamma}{(\gamma - 1)} \log \left(T_2/T_1 \right) - \log(p_2/p_1)$$

$$M_2 = \frac{\sqrt{\frac{\frac{\gamma + 1}{2} M_n^2}{\gamma M_n^2 - \frac{\gamma + 1}{2}}}}{\sin \beta - \theta}$$

The shock polar is formed with the deflection angle on the x-axis and pressure ratio on the y-axis. The reflected shock polar originates at the wedge angle and the triple shock wave point is found at the intersection nearest the 0° deflection angle line of the reflected shock polar and the incident shock polar. There are several different shock reflection possibilities such as Mach reflection with supersonic downstream flow or subsonic downstream flow. Regular reflection is when incoming flow is turned by an incident shock wave by a wedge and reflects off a boundary, the downstream flow can either be super- or sub-sonic. For Mach reflections with supersonic downstream flow, the flow behind the Mach stem is graphed on the incident shock polar between the triple point intersection and the 0° deflection point line. For Mach reflections with subsonic downstream flow, the flow behind the Mach stem is represented by the triple point intersection [10].

The flow downstream can be determined to be super- or sub-sonic by the equation for the Mach number behind the shock wave. Solve for the wedge angle using 1 for M_2 . The asterisk signifies the sonic point on the reflecting shock wave polar. If the triple point intersection is above the asterisk, the flow behind the

reflecting shock wave is subsonic. If the triple point intersection is below the astrisk, the flow behind is supersonic.

$$M_2 = 1 = \frac{M_{n,2}}{\sin \beta - \theta}$$

$$\theta_{\text{sonic}} = \beta - \sin^{-1} M_{n,2}$$

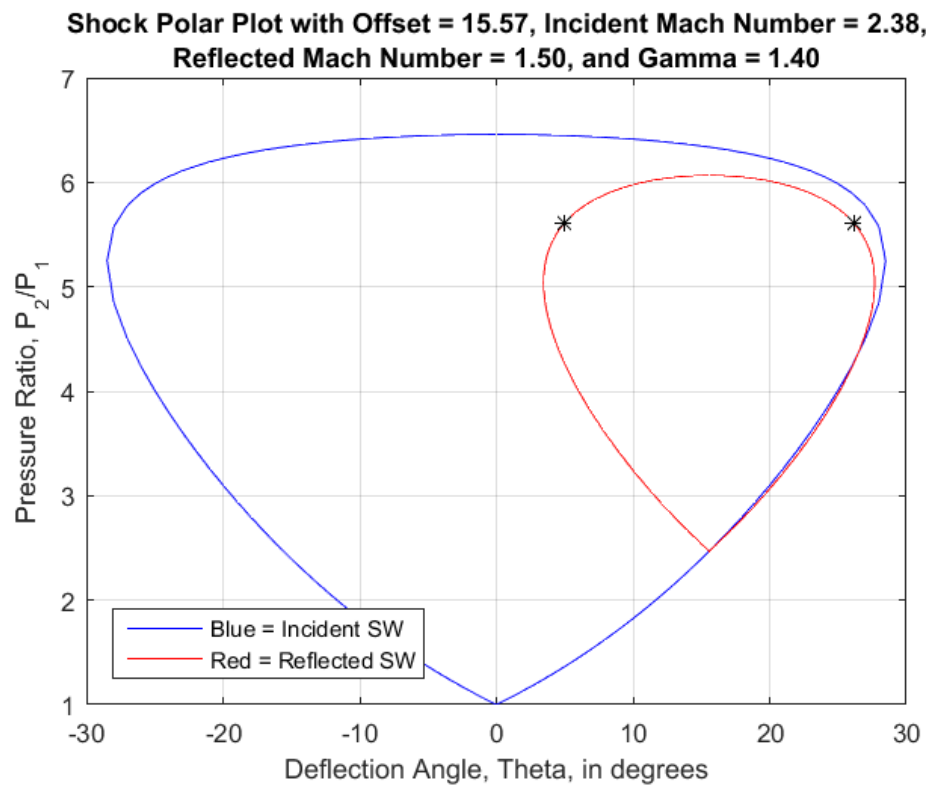


Figure 2-9: Shock polar with initial guess for reflected shock wave

For the incident shock wave Mach number of 2.38 the reflected shock wave Mach number is assumed 1.5. For the Mach reflection in Fig. 2-7 the triple point intersection should appear at angle 3.81° for this shock polar. From Fig. 2-9 the

reflected shock polar does not intersect the incident shock polar, which would indicate no Mach reflection or regular reflection, but this is not the case.

CEA by NASA was used to find the appropriate value for the specific heat ratio, Appendix C has the CEA output [11]. The input for the CEA applet was Fig. 2-9 at wedge angles 15° and 16° and stoichiometric oxidizer to fuel ratios. The output from the applet noted the burned gas specific heat ratio to be 1.13. To understand how the shock polar is affected by Mach number and specific heat ratio a table is constructed to analyze each scenario, see Table 2-2.

Table 2-2: Deflection angles

Image 2	Mach stem angle		
gamma/ Mach	1.597	1.596	1.595
1.14	3.5	3.72	3.89
1.13	3.59	3.81	3.99
1.12	3.68	3.9	4.1

Table 2-2 charts deflection angle possibilities comparing specific heat ratio, along the left side, and Mach number, along the top. The top right and bottom left are at the high and low ends of the spectrum, respectively, while the yellow shaded cell is the deflection angle calculated from Fig. 2-7. The deflection angle varies more rapidly when the Mach number is changed versus when the specific heat ratio is changed. For the original assumption of reflected shock wave Mach number of 1.5 and a 1.4 specific heat ratio the solution does not exist.

The percent change for the pressure and temperature ratios varies depending on the specific heat ratio. Table 2-2 explores the effect of Mach number and specific heat ratio change on the deflection angle, while Table 2-3 looks at the pressure and temperature ratios tabulated against a change in specific heat ratio alone.

Table 2-3: Percent change for calculated variables

Y	Change	P_2/P_1	Change	T_2/T_1	Change
1.11		5.13		1.20	
1.12	0.90%	5.17	0.88%	1.22	1.7%
1.13	0.89%	5.22	0.85%	1.23	1.4%
1.14	0.88%	5.26	0.86%	1.25	1.5%
1.15	0.88%	5.31	0.84%	1.27	1.5%
1.16	0.87%	5.35	0.87%	1.29	1.5%
1.17	0.86%	5.40	0.86%	1.31	1.5%
1.18	0.85%	5.44	0.83%	1.33	1.5%
1.19	0.85%	5.49	0.83%	1.35	1.5%
1.2	0.84%	5.54	0.86%	1.37	1.4%

The change in the specific heat ratio and pressure ratio are less than a percentage point for each specific heat ratio increment. Temperature ratio is between 1.7% and 1.4% points between each step. The derived quantities do not change by a significant amount between each increment of specific heat ratio.

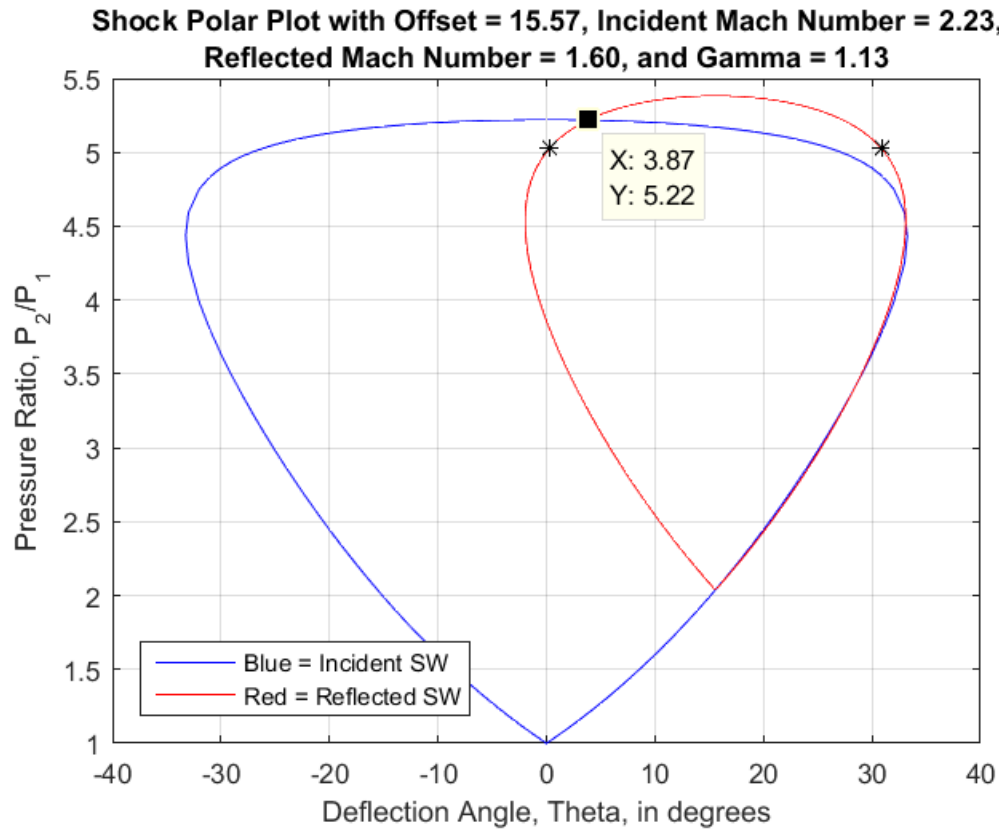


Figure 2-10: Shock polar of Image 2

Above is a shock polar at Mach 1.596 and specific heat ratio 1.13. In Fig. 2-10, the pressure ratio is 5.22 and the deflection angle for the Mach stem is at 3.81. The asterisk is signifying the sonic point of the flow. The triple point intersection in this shock polar is above the sonic point meaning the flow downstream of the reflected shock wave is subsonic and the flow downstream of the Mach stem has the properties of that point. Exploring the flow patterns as they evolve with time will define the Mach number and specific heat ratio more clearly.

Chapter 3: Evolution of Flow

The evolution of the shock wave through time is examined in this Chapter. Starting at the early stages of the shock wave development and ending at the break down of the visible features.

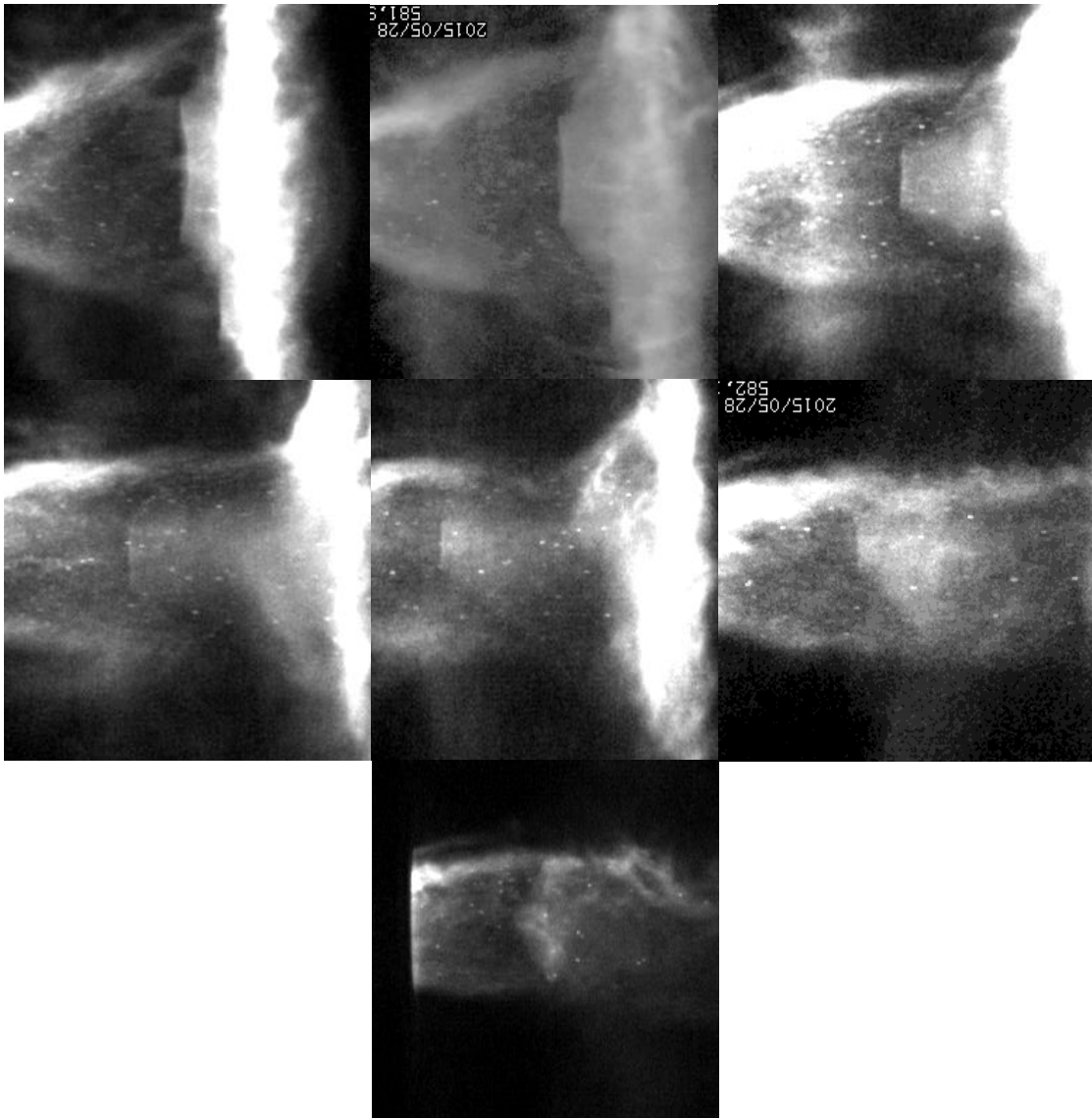


Figure 3-1: Flow evolution images

In Fig. 3-1, the flow patterns evolve with the flow. In the first sub-image the Mach stem is wide and rather angled. In sub-images 2-6 the Mach stem is becoming smaller with larger angles for the lambda feet. Finally in sub-image 7, the Mach stem has disappeared entirely and only the incident shocks remain. This indicates slowing flow because the shock waves are transitioning from stronger to weaker waves. To follow the flow more closely each of these sub-images in Fig. 3-1 has been transformed and examined using the code developed in Chapter 2.

The time stamps for each image in Fig. 3-1 are listed in Table 3-1, all units are in nanoseconds. The total time for all 256 images is 0.0051 seconds, the time from Image 1 to Image 7 is 360,000 nanoseconds. The images were chosen for their clarity of the Mach features and progression through the flow.

Table 3-1: Time stamps for images in flow

Image	1	2	3	4
Time stamp	581952560	581972560	582052560	582092560
Time Difference		20000	80000	40000
Image	5	6	7	
Time stamp	582132560	582192560	582312560	
Time Difference	40000	60000	120000	

3.1 Image 1

The first image can be seen in Fig. 3-2, where the Mach stem is visible as well as the lambda foot. The next image is the post transformation of Fig. 3-2 in Fig. 3-3.

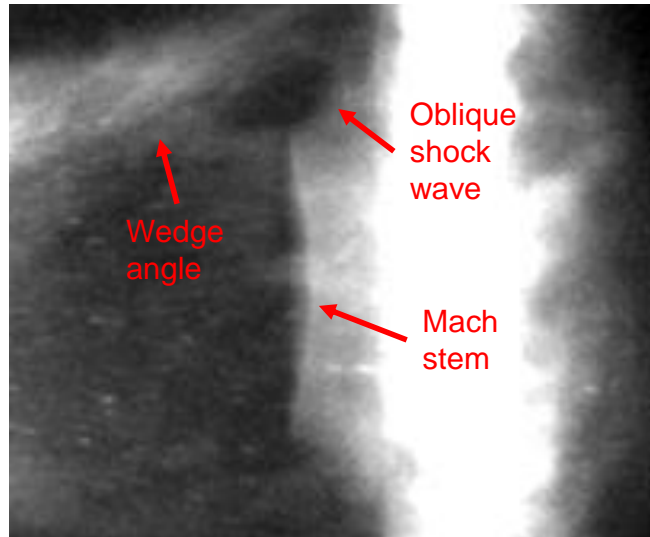


Figure 3-2: Image 1 in flow evolution

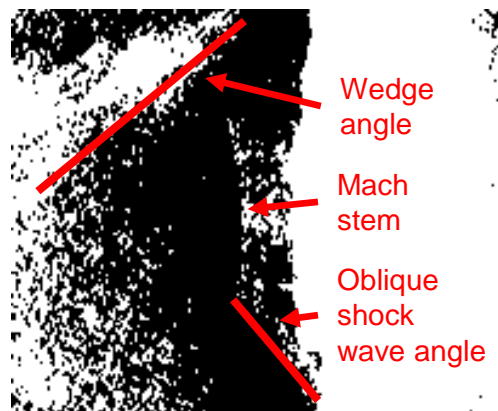


Figure 3-3: Post transform of Fig. 3-2

From Fig. 3-4, the Mach stem is at angle 3.92° , the oblique shock wave is 37.14° , and the wedge angle is 17.6° . A table was compiled like Table 2-2, representing the possible specific heat ratio and Mach number combinations with specific heat ratio along the left side and Mach number along the top. The chart is graphing the Mach stem angles at each scenario, Table 3-2. The yellow shaded cell is the Mach stem angle. Fig. 3-4 is a shock polar of Fig. 3-2 using a reflected shock wave Mach number of 1.666 and a specific heat ratio of 1.13. In Fig. 3-4 the sonic point, noted by the asterisk, is below the triple point shock intersection meaning the flow behind the reflected shock is subsonic.

Table 3-2: Shock polar results of Image1

Image 1	Mach stem angle		
Gamma/ Mach	1.667	1.666	1.665
1.14	3.54	3.76	3.92
1.13	3.67	3.92	4.07
1.12	3.72	3.99	4.16



Figure 3-4: Shock polar of Fig. 3-2

3.2 Image 2

Next is the second image in the flow evolution, however this image was used in the previous Chapter to demonstrate the code, refer to Chapters 2-2 and 2-3.

3.3 Image 3

The third image in the flow evolution is represented in Fig. 3-5.

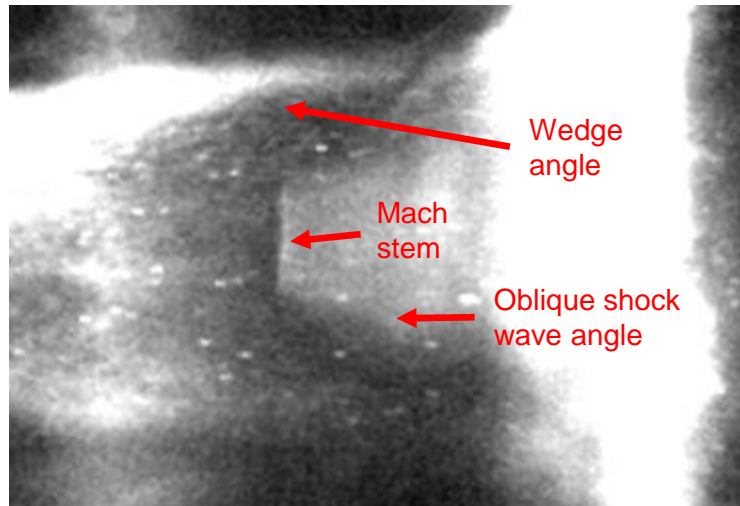


Figure 3-5: Image 3 in flow evolution

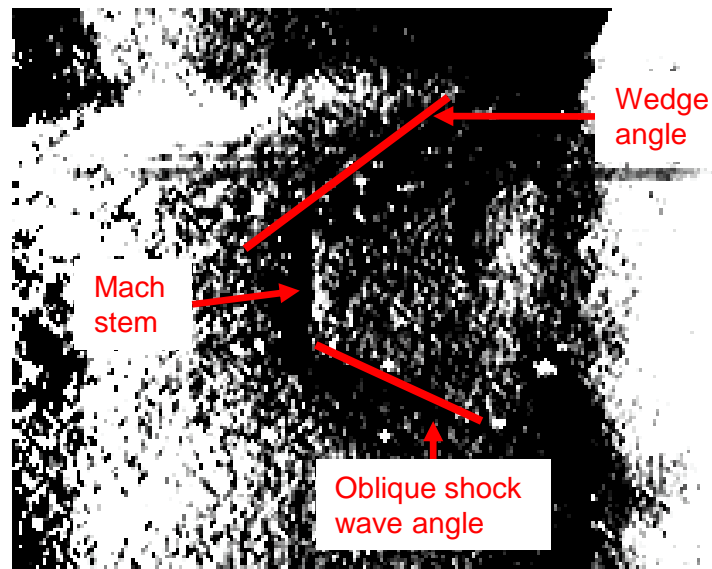


Figure 3-6: Post transform Fig. 3-5

In Fig. 3-5 the Mach stem is getting smaller and less angled, while the oblique shock waves are becoming more elongated. Fig. 3-6 is the post transformation image of Fig. 3-5. From Fig. 3-6, the Mach stem angle is 3.18° , the oblique shock wave angle is 25.82° , and the wedge angle is 11.48° . A shock polar table has been formulated, see Table 3-3.

Table 3-3: Shock polar results of Image 3

Image 3	Mach stem angle		
gamma/ Mach	2.272	2.2708	2.27
1.14	-0.4	0.89	1.8
1.13	1.59	3.18	4.38
1.12	4.18	6.36	8.16

In Table 3-3, the yellow shaded cell is the correct Mach stem angle. Fig. 3-7 is the shock polar of Table 3-3 using a specific heat ratio of 1.13 and a reflected shock wave Mach number of 2.2708. The sonic point is below the triple point intersection therefore the flow is subsonic after the reflected shock wave.



Figure 3-7: Shock polar of Image 3

3.4 Image 4

The fourth image in the evolution is in Fig. 3-8. The Mach stem is starting to fade as well as the oblique shock waves and wedge angles.

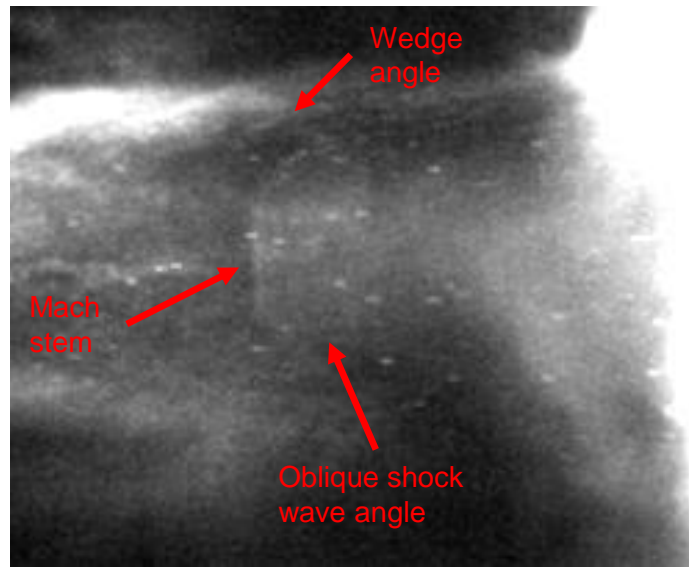


Figure 3-8: Image 4 in flow evolution

Fig. 3-9 is the post transformation image of Fig. 3-8. From Fig. 3-9, the Mach stem angle is 4.40° , the oblique shock wave angle is 40.82° , and the wedge angle is 12.36° . Table 3-4 is the shock polar chart representing all possible solutions for Image 4 of the flow evolution.

Table 3-4: Shock polar results of Image 4

Image 4	Mach stem angle		
gamma/ Mach	1.532	1.5311	1.53
1.14	4.04	4.29	4.55
1.13	4.16	4.4	4.7
1.12	4.3	4.58	4.86

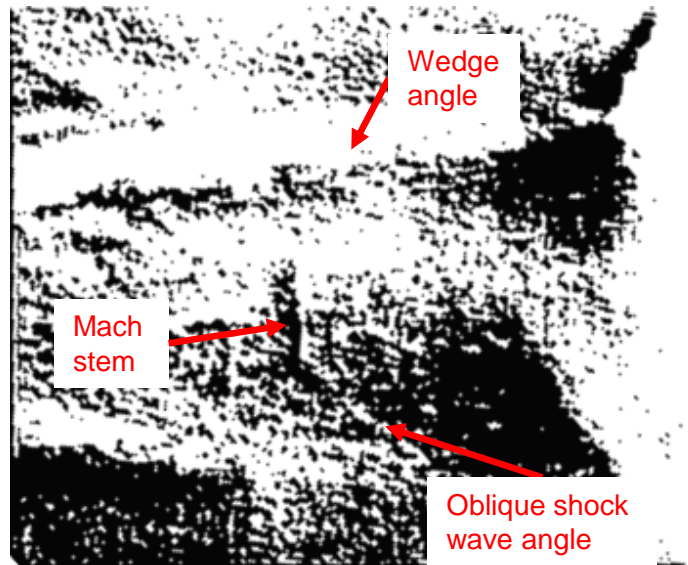


Figure 3-9: Post transform Fig. 3-8

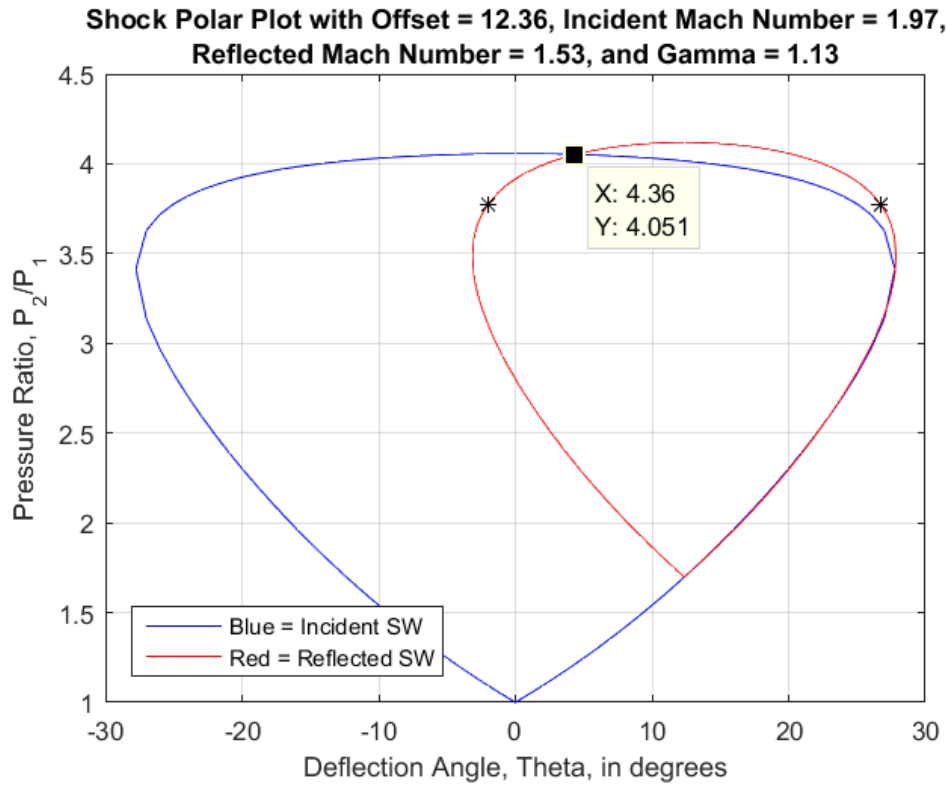


Figure 3-10: Shock polar of Image 4

Table 3-4 describes the still slowing nature of the flow, the yellow shaded cell is the Mach stem angle. Fig. 3-10 is a shock polar of Image 4 at specific heat ratio 1.13 and a reflected shock wave Mach number of 1.5311. The flow is subsonic passed the reflected shock wave.

3.5 Image 5

The fifth image in the flow evolution is Fig. 3-11.

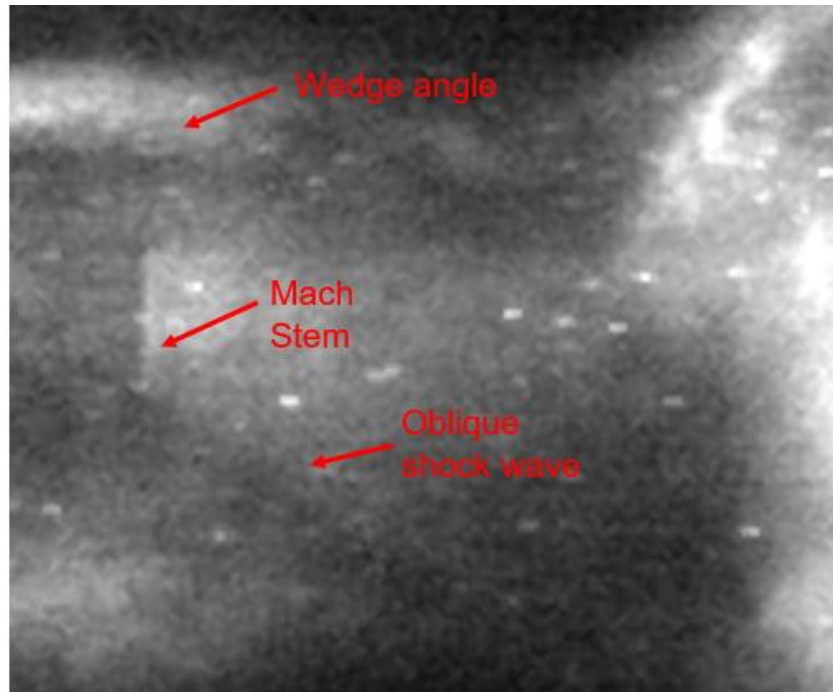


Figure 3-11: Image 5 of flow evolution

In Fig. 3-11, the Mach stem, oblique shock wave, and wedge angle are continuing to get less pronounced. Fig. 3-12 is the post transformed image of Fig. 3-10. Fig. 3-12 is rotated to focus on the oblique shock wave angle and the wedge angle. The Mach stem angle is 3.58° , the oblique shock wave angle is 32.83° , and the wedge angle is 12.36° . Table 3-5 is the shock polar results chart for Image 5. Fig. 3-13 is a shock polar of Image 5 with specific heat ratio 1.13 and a reflected

shock wave Mach number of 1.8332. The flow is subsonic passed the reflected shock wave.

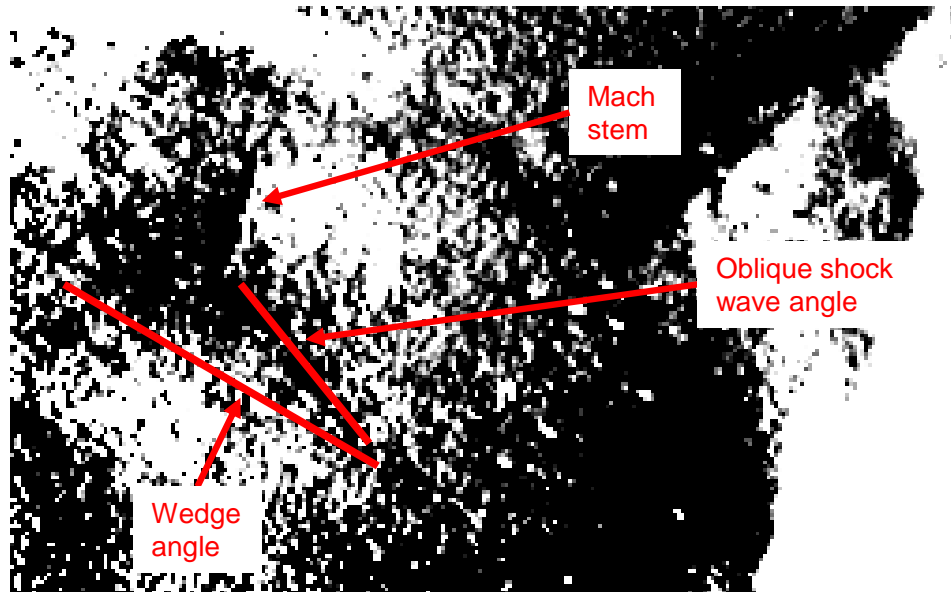


Figure 3-12: Post transform Fig. 3-10

Table 3-5: Shock polar results of Image 5

Image 5	Mach stem angle		
gamma/ Mach	1.834	1.8332	1.832
1.14	2.56	3	3.71
1.13	3.1	3.58	4.35
1.12	3.71	4.24	5.1

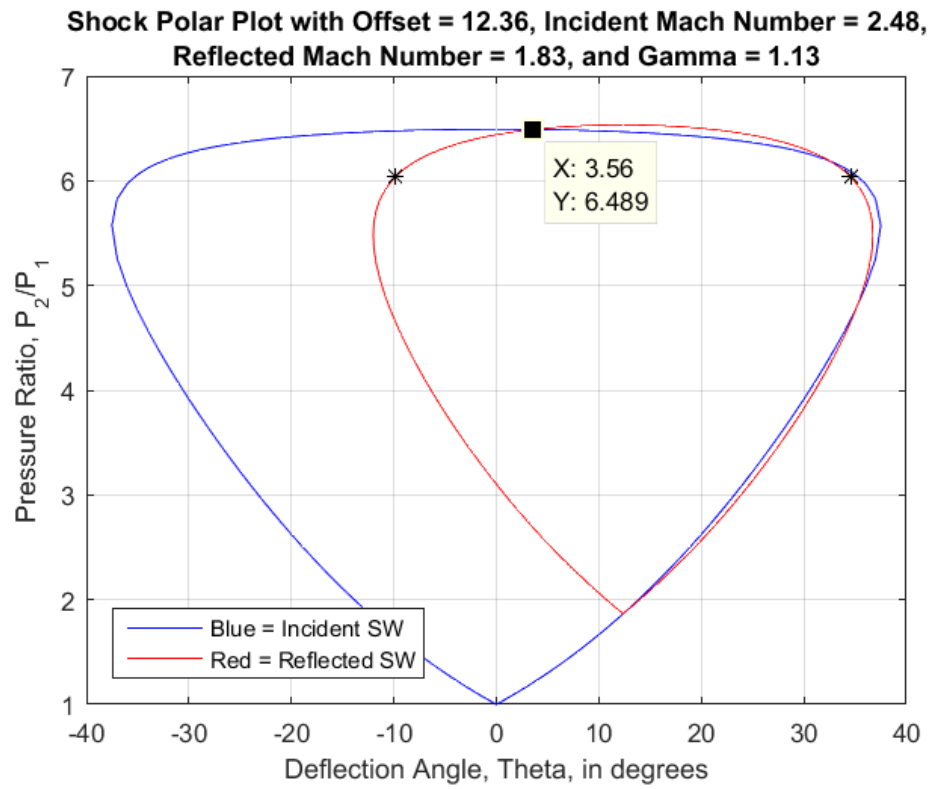


Figure 3-13: Shock Polar of Image 5

3.6 Image 6

Fig. 3-14 is Image 6 in the flow evolution.

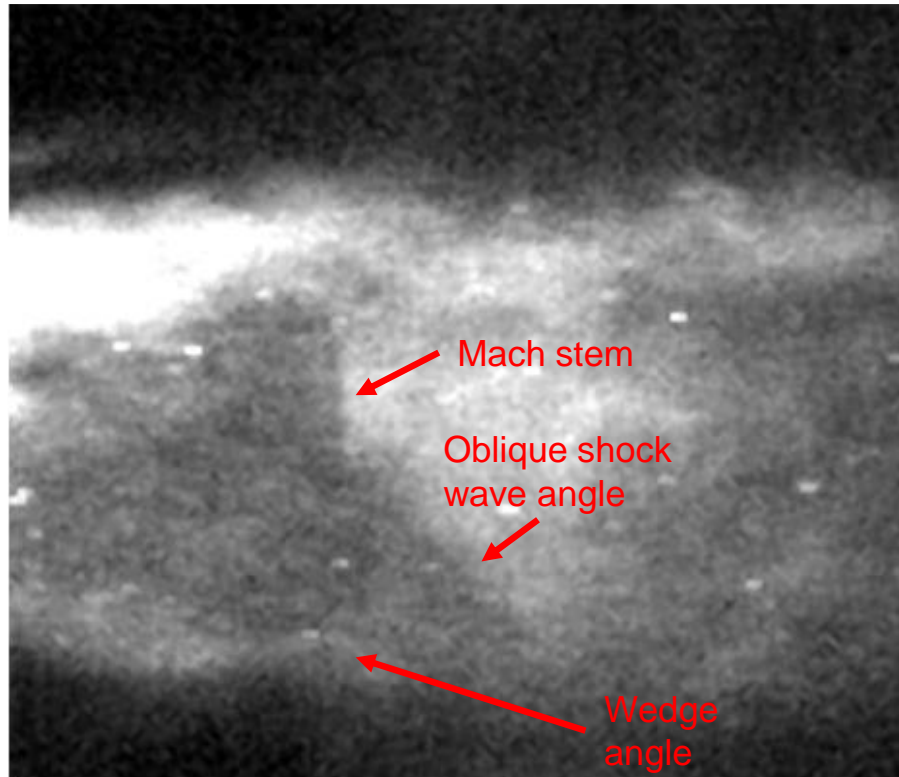


Figure 3-14: Image 6 in flow evolution

In Fig. 3-13, the Mach stem, oblique shock wave, and wedge angle are continuing to get less pronounced, the upper lambda foot has been hidden from view. Fig. 3-15 is the post transformed image of Fig. 3-14.

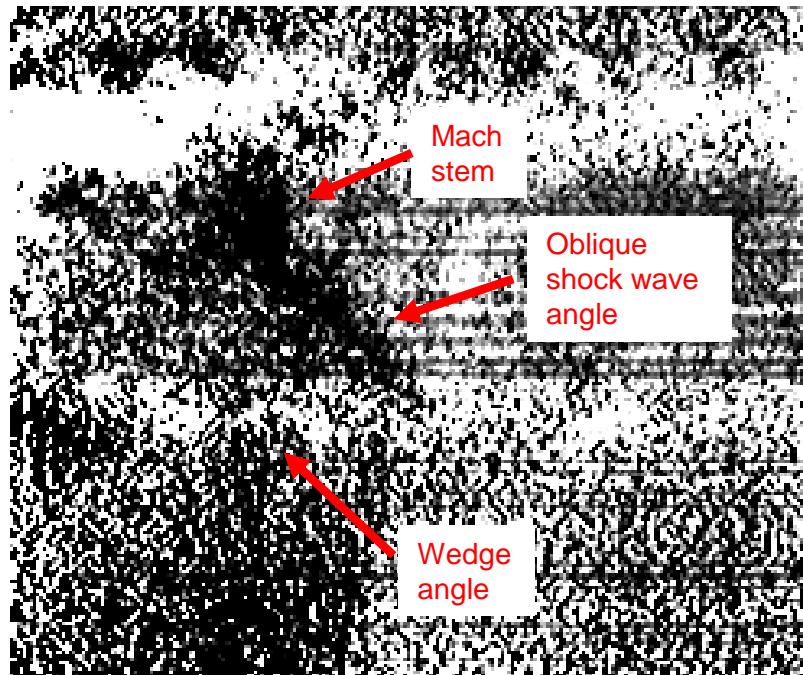


Figure 3-15: Post transform of Fig. 3-14

From Fig. 3-15, the Mach stem angle is 4.40° , the oblique shock wave angle is 38.45° , and the wedge angle is 10.20° . Table 3-6 is the shock polar results chart for Image 5. Fig. 3-16 is a shock polar of Image 6 with specific heat ratio 1.13 and a reflected shock wave Mach number of 1.6019 with subsonic flow behind the reflected shock wave.

Table 3-6: Shock polar results of Image 6

Image 6	Mach stem angle		
gamma/ Mach	1.61	1.6019	1.6
1.14	1.18	4.26	5.18
1.13	1.19	4.4	5.35
1.12	1.45	4.9	5.94

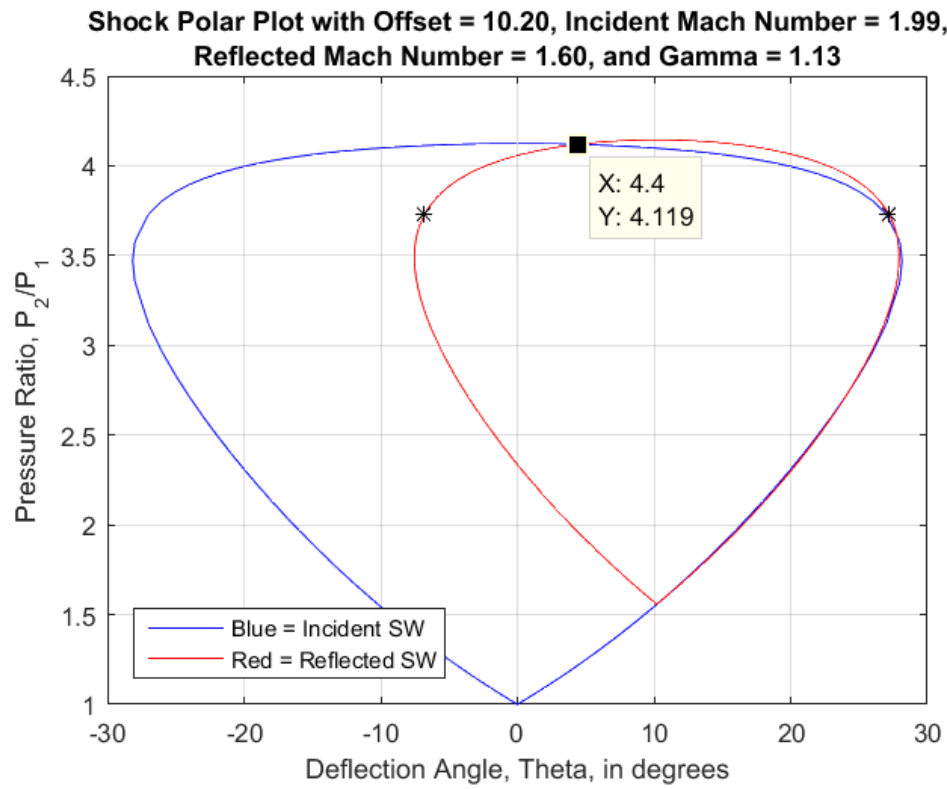


Figure 3-16: Shock polar of Image 6

3.7 Image 7

Fig. 3-17 is the final image in the flow evolution. In this image the Mach stem has disappeared and the oblique shock waves and wedge angles are the remaining features.

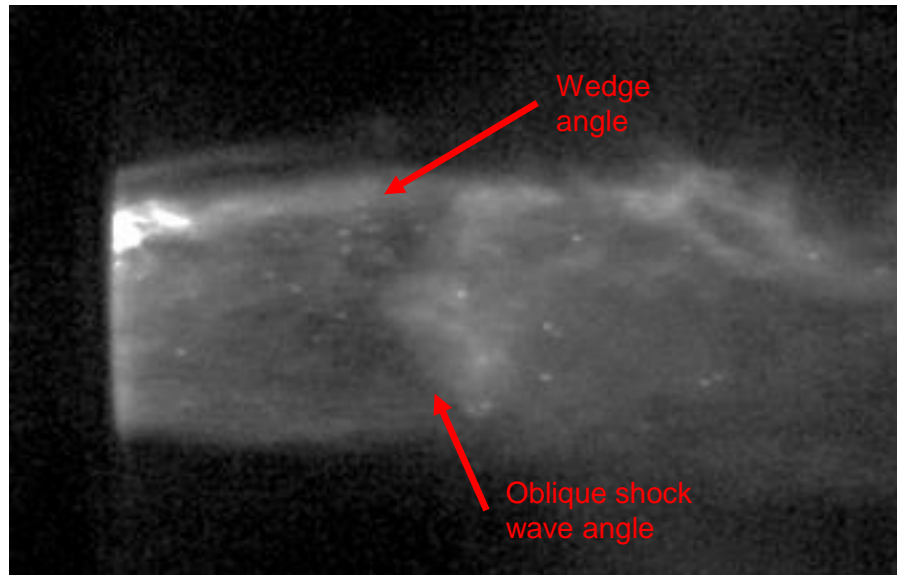


Figure 3-17: Image 7 in flow evolution

Fig. 3-19 is the post transformed image of Fig. 3-17. The oblique shock wave angle is 37.41° and the wedge angle is 10.86° . The Mach stem has disappeared so there is no triple point, but there is still a Mach reflection. The flow after it passes through the incident oblique shock wave still needs to turn back to parallel to the free-stream flow. Fig. 3-18 depicts the flow going through the incident and reflected shock waves.

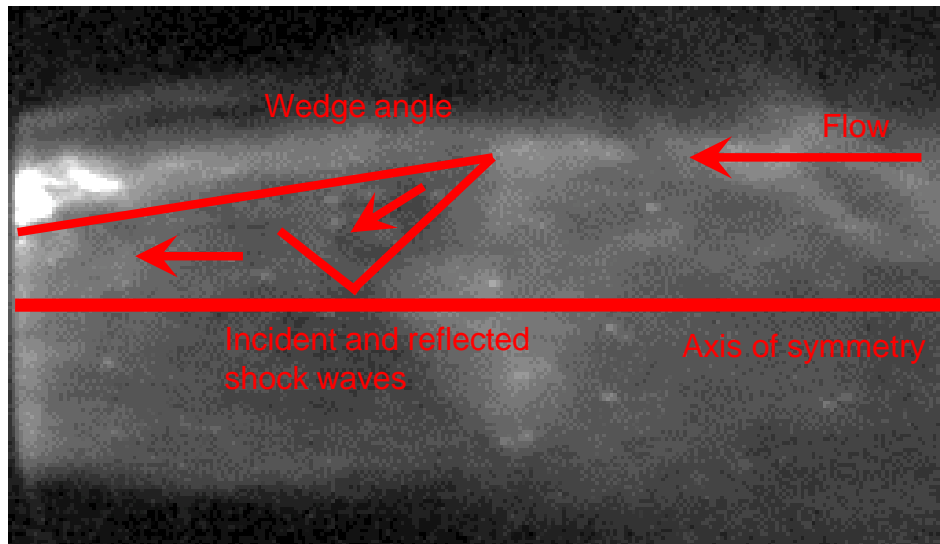


Figure 3-18: Mach reflection with no triple point

Fig. 3-19 is the post transform image of Fig. 3-17. For the previous 6 images the shock polar intersection nearest the zero deflection line was the triple point intersection, but Image 7 does not have a Mach stem. For a regular reflection, not a Mach reflection, the point of reflection on a shock polar is when the reflected shock polar crosses the zero deflection line [10]. The shock polar crosses at Mach 1.65 because that Mach number and specific heat ratio intersect at the 0 deflection angle line. Since there is no Mach stem, the incident shock wave is gaining a higher Mach number, but the Mach number behind the reflected shock wave is still subsonic. Table 3-7 is a Table shock polar results for Image 7. Fig. 3-20 is the shock polar for reflected Mach number 1.651 and specific heat ratio 1.13.

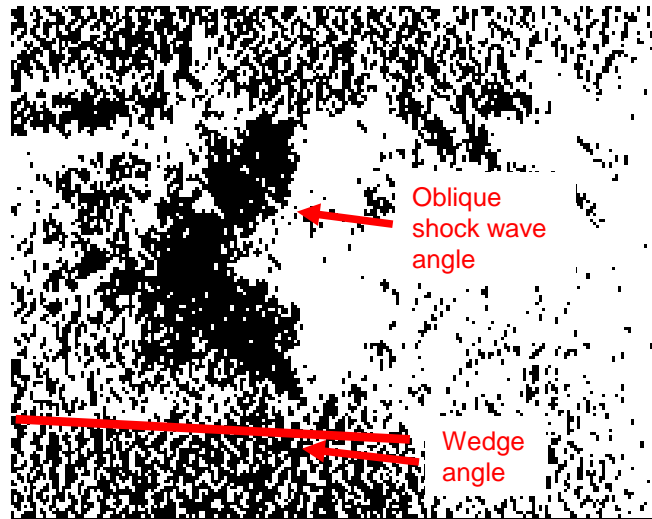


Figure 3-19: Post transform of Fig. 3-17

Table 3-7: Shock polar results for Image 7

Image 7	Mach stem angle		
gamma/ Mach	1.652	1.65135	1.65
1.14	-0.46	-0.3	0.1
1.13	-0.196	0	0.4
1.12	-0.1	0.1	0.57

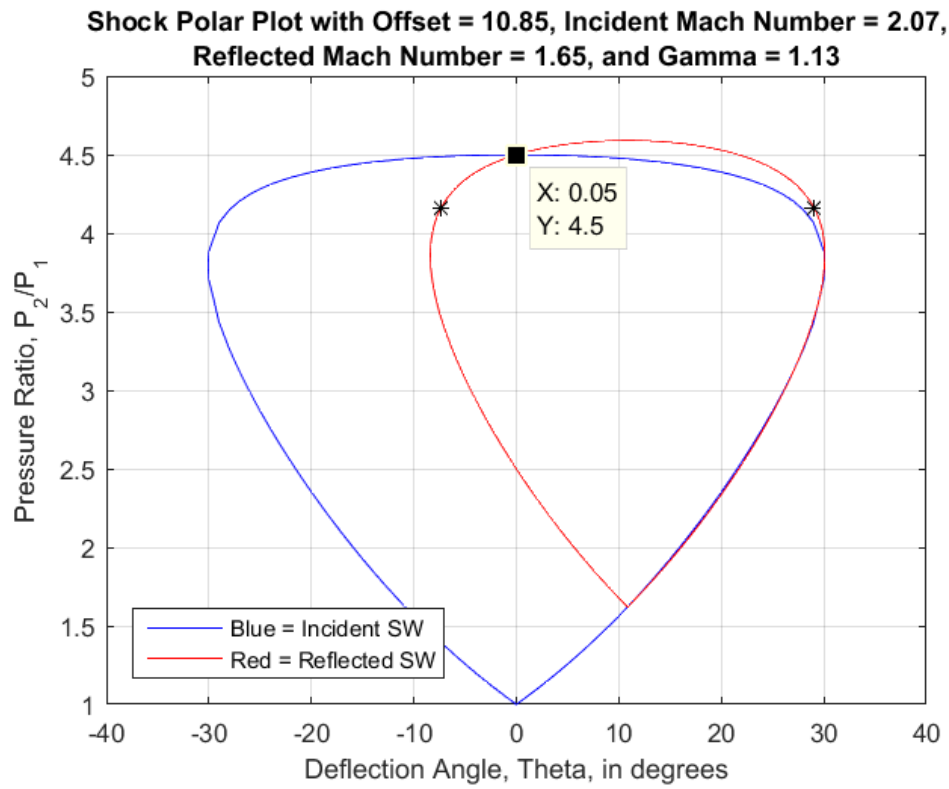


Figure 3-20: Shock polar for Image 7

3.8 Velocity Calculations

From Chapter 2.1, the PDE tube was seeded with titanium dioxide, TiO_2 , nanoparticles. These particles can be seen and tracked in each image. Fig. 3-20 has particles identified in the image, however there are many more particles than the ones specifically indicated. These particles were identified and tracked to find displacement from image to image, and combined with the time stamps on each image, the velocity was calculated. Additional images were used from the 256 image series to make the particle tracking more accurate. Starting with one image prior to Image 1 in Chapter 3.1, each image is 20,000 nanoseconds apart, the last image used in the particle tracking is Image 7 from Chapter 3.7. There are a total of 20 images used for particle tracking.

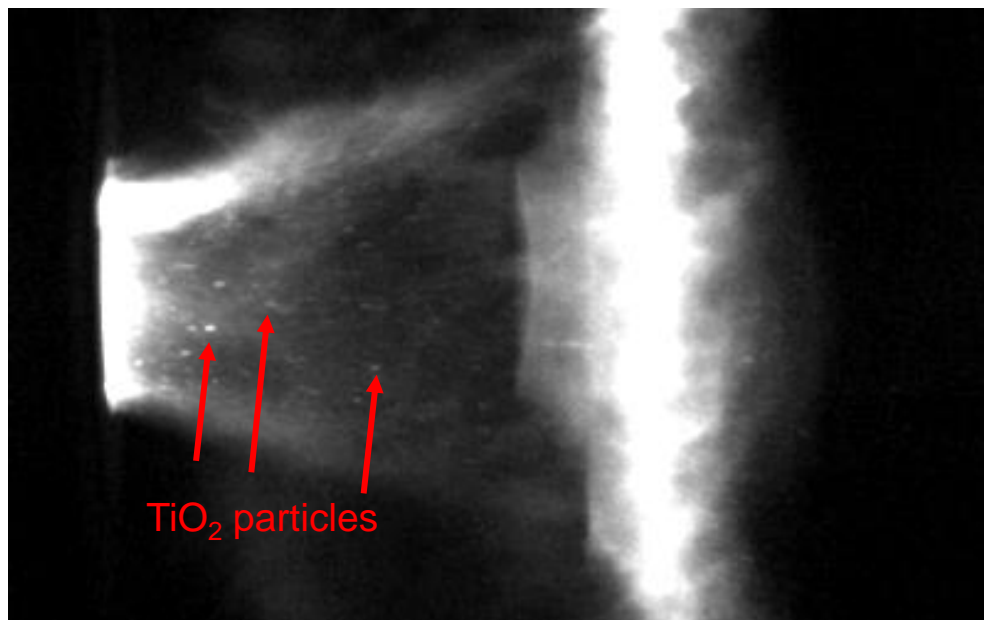


Figure 3-21: TiO_2 nanoparticle identification

Fig. 3-22 is the first image for particle tracking. The 2 particles selected are towards the PDE tube in the lower half of the flow and highlighted by a red circle.

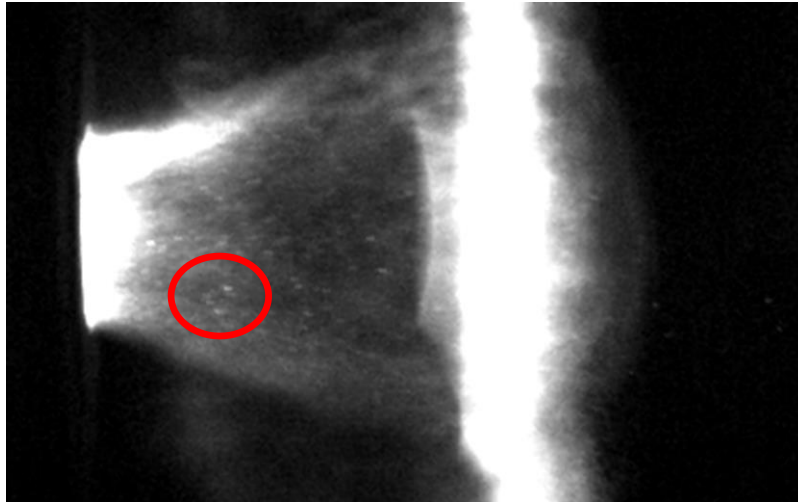


Figure 3-22: Particle tracking image at 0 ns

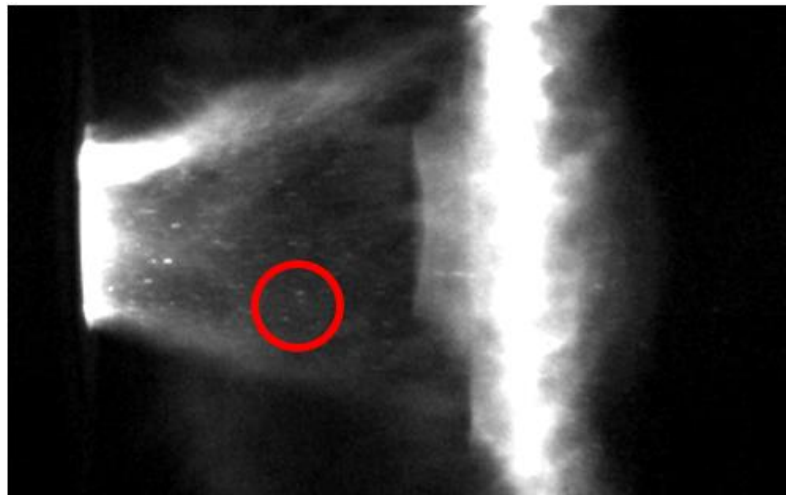


Figure 3-23: Particle tracking image at 20,000 ns

To track the particles through the images, the pixel coordinates were noted along their path and triangulated to find the length traveled. The distance was found using the pixel to millimeter ratio from Chapter 2.2, which is 2. Once the coordinates are known, the length between the 2 positions of the particle is found. Then the length is divided by the time between images to find the velocity. To find the length the equation below was used,

$$\text{Total Legnth} = \sqrt{\left(\frac{X_2 - X_1}{2}\right)^2 + \left(\frac{Y_2 - Y_1}{2}\right)^2}$$

Table 3-8 is a Table denoting the coordinates of the pixels, length traveled, and the velocity. Total length is in millimeters, velocity in meters per second, and time is 20,000 nanoseconds.

Table 3-8: Length and velocity calculation

0 ns	X-Coord	Y-Coord	20k ns	X-Coord	Y-Coord	Tot. Length	Velocity
Particle 1	111	142	Particle 1	148	146	18.6	930
Particle 2	104	154	Particle 2	142	158	19.1	955

From Table 3-8, the velocity of the 2 particles from 0 to 20,000 ns is 930.4 m/s for Particle 1 and 955.25 m/s for Particle 2. In Figs. 3-22 and 3-23 the particles are moving from the front end of the flow to the middle of the flow. The position of the particle in the flow indicates relative speed. The particles nearest the PDE tube are slowest and speed up the closer they get to the shock wave. From Fig. 2-8, the incident shock wave is the oblique shock wave extending from the wedge angle, and the reflected shock wave is the assumed shock wave reflecting from the triple point into the flow towards the PDE tube. So the flow going slower towards the

PDE tube is an indication of the reflecting shock wave slowing down the flow. The particles are charted in a table with placement along the top and time along the left side. Table 3-9 is an abbreviated to show the velocities for each particle, the entire table with coordinates is in Appendix C.

Table 3-9: Particle velocities

Velocity of particles charted on placement vs time in m/s								
Time ns	PDE tube		Middle		Near shock wave		On s.w.	
0-20K		955.2	930.4					
20-40k			966.0	1025.0				
40-60k					1060.7		1126.1	
60-80k			937.1	875.4	925.0			
80-100k					958.2	955.2		903.1
100-120k						1076.2	951.3	1050.0
120-140k	650.5	800.0	825.0					
140-160k			776.6	876.4	850.4			
160-180k				850.4			875.0	900.3
180-200k	701.8		977.9					
200-220k			775.4				1100.3	
220-240k				751.7				
240-260k	625.0							
260-280k			651.9					
280-300k					651.9			
300-320k			579.9				825.4	
320-340k			600.0			600.5		
340-360k			750.4				600.0	
360-380k		704.0				725.0		

Table 3-10 describes what time stamp each of the images in Chapters 3.1

- 3.7 are with respect to the particle tracking in Table 3-9.

Table 3-10: Time for each flow evolution image

Image	1	2	3	4	5	6	7
Time ns	20k	40k	120k	160k	200k	260k	380k

From Table 3-9 the velocity is fastest from 60 – 120k ns, slows down from 140 – 320k ns, and then speeds back up between 340 - 380k ns. This agrees with the analysis in Chapters 3.1 – 3.7. Image 1 through Image 7 all have subsonic flow downstream of the reflected shock waves. The disappearance of the Mach stem in Image 7 leads to the flow speeding back up. Table 3-11 is comparing the Mach numbers for the incident and reflected shock waves in Chapters 3.1 – 3.7.

Table 3-11: Incident and reflected shock wave Mach number

Image	Incident	Reflected
1	2.51	1.67
2	2.23	1.6
3	3.25	2.27
4	1.97	1.53
5	2.48	1.83
6	1.99	1.6
7	2.07	1.65

Image 5 has an incident shock wave Mach number of 2.48 where Images 4 and 6 are 1.97 and 1.99, respectively. In Table 3-9 the velocity increases in the time slot of 180 – 200k ns and middle flow to 977.9 m/s, which is the time stamp of Image 5.

Chapter 4: Conclusion

This work is the summation of numerical evaluation of images taken at the Aerodynamics Research Center. The research analyzed Mach features in unsteady flow exiting a supersonic nozzle. In order to gain more insight in the interactions of the Mach features of the shock diamonds, a method was developed to process the images to find the locations of shock waves, then plotting the results in a shock polar.

This method highlights the options using Abel transforms and computer automation in image processing. After analyzing images in the flow evolution using the methods developed, the velocity was calculated tracking particle that were seeded in the flow. The comparison revealed the Abel transform and shock polar had successfully obtained the Mach number and heat ratio. From the Mach number and heat ratio other properties of the shock wave can be found.

Numerical integration could be incorporated into the Abel transform code in Matlab. This would decrease computation time spent by the computer transforming the images. Other ways to further this research would be to have the computer determine the angles by taking measures of the Mach features and inputting those angles to the shock polar code.

References

- [1] J. D. Anderson and Jr., Fundamentals of Aerodynamics, New York, NY: McGraw Hill, 2007.
- [2] M. J. Zucrow and J. D. Hoffman, Gas Dynamics Volume 1, John Wiley & Sons, Inc., 1976.
- [3] H. Liepmann and A. Roshko, Elements of Gasdynamics, New York, NY: John Wiley & Sons, Inc., 1957.
- [4] F. K. Lu, D. D. Joshi, J. T. Peace, R. T. Bello and J. D. Carter, "Flow visualization of the exhaust jet from a pulse detonation engine by Mie scattering," in *30th International Symposium on Shock Waves*, Tel Aviv, Israel, 2015.
- [5] C. Killer, "MathWorks File Exchange," 26 September 2013. [Online]. Available: <http://www.mathworks.com/matlabcentral/fileexchange/43639-abel-inversion-algorithm>. [Accessed 15 08 2015].
- [6] R. N. Bracewell, The Fourier Transform and It's Applications, Singapore: McGraw Hill, 2000.
- [7] G. Pretzler, "A New Method for Numerical Abel-Inversion," *Z. Naturforsch*, vol. 46a, pp. 639-641, 1991.

- [8] A. R. Collar, "Iterative Solutions of the Equations for Plane Oblique Shock Waves," *Journal of the Royal Aeronautical Society*, vol. 63, no. 587, pp. 669-672, 1959.
- [9] H. Hornung, "Regular and Mach Reflections of Shock Waves," *Annual Review of Fluid Mechanics*, vol. 18, pp. 33-58, 1986.
- [10] C. A. Mouton, "Transition between Regular Reflection and Mach Reflection in the Dual-Solution Domain," California Institute of Technology, Pasadena, CA, 2007.
- [11] MathWorks, "Matlab User Guide," MathWorks, [Online]. Available: <http://www.mathworks.com/help/matlab/>. [Accessed 2015-2016].
- [12] M. Kurosaka and N. Tsuboi, "Spinning Detonation, Cross-Currents, and the Chapman-Jouguet Velocity," *Journal of Fluid Mechanics*, vol. 756, pp. 728-757, 2014.
- [13] "Chemical Equilibrium with Applications," National Aeronautics and Space Administration, 4 February 2016. [Online]. Available: <http://www.grc.nasa.gov/WWW/CEAWeb/>. [Accessed 11 April 2016].

Appendix A: Inverse Able Transform Code

```
function [ ] = loopabel(h,R,upf)

%Loopabel function takes an image and performs an inverse
Abel transform.
%The inputs are...
%
%h   = image to be transformed
%R   = length of matrix h
%upf = cosine frequency limit

h = imread('Camera_15_17_55_034.tiff');
h = fliplr(h);
g0 = im2double(h);
g1 = g0(:, :, 1);

R = size(g1,2); %pixels

Aud1 = zeros(size(g1,1),size(g1,2));
j = 1;
while j < size(g1,1);
    v=g1(j,:);
    [ f_rec1 , X1 ] = abel_inversion(v,upf,R);
    opl=(f_rec1./max(f_rec1))';
    Aud1(j,:)=opl;
    j=j+1;
end

imshow(Aud1)
```

```

function [ f_rec, X ] = abel_inversion(h,upf,R)

X=linspace(0,R-0.01,length(h))';

% calculate series expansions fn and corresponding
% integrals hn
% allocate matrices for f_n and h_n - rows are x-values,
% columns are the number of expansion elements (n+1 since
% we start with n=0)
fn=zeros(length(X),upf+1);
hn=zeros(length(X),upf+1);

% special case: first column for n=0, where f_0(r)=1;
fn(:,1)=1;
for c=1:length(X);
    x=X(c);

    % evaluation of (3)
    fun=@(r) r./sqrt(r.^2-x.^2);
    hn(c,1) = integral(fun,x,R);
end

% all the other columns
for n=1:upf
    for c=1:length(X)
        x=X(c);

        % evaluation of (2)
        fn(c,n+1) = (1 - (-1)^n*cos(n*pi*x/R));

        % evaluation of (3)
        fun=@(r) (1 - (-1)^n*cos(n*pi*r/R)).*r./sqrt(r.^2-
x.^2);
        hn(c,n+1) = integral(fun,x,R);
    end
end

B = zeros(1,upf+1); L = zeros(upf+1,upf+1); %create arrays

for k=1:upf+1

    for l=1:upf+1
        L(l,k)=sum(hn(:,k).*hn(:,l));
    end
end

```



```

    B(k)=sum(h(:).*hn(:,k));
end

    A=B/L;

% final stage: calculate the resulting distribution profile

% create vector for resulting reconstructed distribution
f_rec=zeros(length(h),1);

% special case for n=0 (where f_0(r) = 1)
f_rec = f_rec + A(1)*1;

% iterate eq. (1) for n=1:upf
for c=2:upf+1
    f_rec = f_rec + A(c).*fn(:,c);
end

```

Appendix B: Shock polar Code

```
function [ ] = PolarPlot(beta, theta, g, RSW, Table)

%This function creates a shock polar of a triple point
shock intersection.
%The graphed equations on the chart are the incident shock
wave in blue and the
%reflected shock wave in red. The sonic point is calculated
and highlighted
%by an asterisk on the reflected shock wave line. The
triple point is the
%intersection of the reflected shock wave line with the
incident shock wave
%line nearest the zero deflection angle. This function uses
Collar's
%Theorem for solving oblique shock waves iteratively.
% A. R. Collar, "Iterative Solutions of the Equations for
Plane Oblique
% Shock Waves," Journal of the Royal Aeronautical
Society, vol. 63, no.
% 587, pp. 669-672, 1959.
%
%The inputs are...
%
%beta = Incident Shock Wave Angle
%theta = Wedge Angle
%RSW = Reflected Shock Wave Mach Number, if it is unknown
guess
%Table = 1 or 0, 1 if you want an excel workbook of the
properties of the
% ISW and RSW, 0 if not.

if ~exist('Table', 'var'); Table=0; end;

b = beta; % Wave Angle in degrees
d_os = theta; % Wedge Angle in degrees
tt = tand(d_os); % tan(wedge angle)
M = 0; % Starting Mach number for Incident
Shock Wave
t = 0; % Starting condition to find the Mach
number for ISW

while t <= tt
```

```

t = 2*cotd(b)*(M^2*sind(b)^2-1)/(M^2*(g+cosd(2*b))+2);
if t<= tt
    M = M + 0.001;
else
    M1 = M;
end

end

M1_2 = RSW;          %Reflected Shock Wave Mach Number

%Collar's Theorem for the Offset
A = M1^2-1;
B_os = (g+1)/2*M1^4*tan(pi/180*(d_os));
C_os = ((g+1)/2*M1^2+1)*tan(pi/180*(d_os));

i_os = 2;
x_os = zeros(1, 50);

x_os(1,1) = sqrt(M1^2-1);
x_os(1,2) = sqrt(A - B_os/(C_os+x_os(1,1)));
for i_os = 2:50
    x_os(1,(i_os+1)) = sqrt(A - B_os/(C_os+x_os(1,i_os)));
end

beta_i = 90-180/pi*(atan(x_os(end)));
Mn_i = M1*sin(pi/180*(beta_i));
p_os = (2*g*Mn_i^2-(g-1))/(g+1);
r_os = (g+1)*Mn_i.^2/(2+(g-1)*Mn_i.^2);

%For the Incident Shock Wave
%To find the max beta angle, max normal Mach number, and
theta vector
beta_max = 180/pi*(asin(sqrt((1/(g*M1^2))*(0.25*(g+1)*M1^2-
1+sqrt((g+1)*(1+0.5*(g-1)*M1^2+(g+1)/16*M1^4))))));
Mn_max = M1*sin(pi/180*(beta_max));
theta_betamax =
180/pi*(atan(1/(tan(pi/180*(beta_max)))*(Mn_max^2-
1)/(0.5*(g+1)*M1^2-Mn_max^2+1))));
theta1 = (0:theta_betamax);
theta2 = fliplr(theta1);
theta = horzcat(theta1,theta_betamax,theta2); %in
degrees
theta_n = theta*-1;

z = size(theta);

```

```

%Collar's Theorem for ISW
B = (g+1)/2*M1^4*tan(pi/180*(theta));
C = ((g+1)/2*M1^2+1)*tan(pi/180*(theta));

i = 2;
j = 1;
x = zeros(z(2), 50);

for j = 1:z(2)
    x(j,1) = sqrt(M1^2-1);
    x(j,2) = sqrt(A - B(1,j)/(C(1,j)+x(j,1)));
    for i = 2:50
        x(j,(i+1)) = sqrt(A - B(1,j)/(C(1,j)+x(j,i)));
    end
end

%To calculate the beta vector
r = size(theta);
beta1 = zeros(1,r(2));
beta2 = zeros(1,r(2));
h = 1;
e = 1;

for h = 1:z(2)
    if h <= r(2)
        beta1(1,h) = 90 - 180/pi*(atan(x(h,51)));
    else if h == r(2)+1
        beta_max;
    else if h >= r(2)+2
        beta2(1,e) = 180/pi*(atan(1/(0.5*(-
(C(1,h)+x(h,51))+sqrt((C(1,h)+x(h,51))*(C(1,h)-
3*x(h,51))+4*A)))));
        e = e+1;
    end
end
end
end

beta = horzcat(beta1,beta_max,beta2);

%To calc the Mn vector, pressure, temp, and density ratios,
Mach 2 vector,
%and the del(s)/R vector
Mn = M1*sin(pi/180*(beta));
p2p1 = (2*g*Mn.^2-(g-1))/(g+1);

```

```

r2r1 = (g+1)*Mn.^2./(2+(g-1)*Mn.^2);
T2T1 = p2p1./r2r1;
dsR = g/(g-1)*log(T2T1)-log(p2p1);
Mn2 = sqrt((1+0.5*(g-1)*Mn.^2)./(g*Mn.^2-0.5*(g-1)));
M2 = Mn2./sin(pi/180*(beta-theta));

%For the Reflected Shock Wave
%To find the max beta angle, max normal Mach number, and
theta vector
beta_max_2 =
180/pi*(asin(sqrt((1/(g*M1_2^2))*(0.25*(g+1)*M1_2^2-
1+sqrt((g+1)*(1+0.5*(g-1)*M1_2^2+(g+1)/16*M1_2^4))))));
Mn_max_2 = M1_2*sin(pi/180*(beta_max_2));
theta_betamax_2 =
180/pi*(atan(1/(tan(pi/180*(beta_max_2)))*(Mn_max_2^2-
1)/(0.5*(g+1)*M1_2^2-Mn_max_2^2+1))));
theta1_2 = (0:0.1:theta_betamax_2);
theta2_2 = fliplr(theta1_2);
theta_2 = horzcat(theta1_2,theta_betamax_2,theta2_2);
%in degrees

z_2 = size(theta_2);

%Collar's Theorem for the RSW
A_2 = M1_2^2-1;
B_2 = (g+1)/2*M1_2^4*tan(pi/180*(theta_2));
C_2 = ((g+1)/2*M1_2^2+1)*tan(pi/180*(theta_2));

i_2 = 2;
j_2 = 1;
x_2 = zeros(z_2(2), 50);

for j_2 = 1:z_2(2)
    x_2(j_2,1) = sqrt(M1_2^2-1);
    x_2(j_2,2) = sqrt(A_2 -
B_2(1,j_2)/(C_2(1,j_2)+x_2(j_2,1)));
    for i_2 = 2:50
        x_2(j_2,(i_2+1)) = sqrt(A_2 -
B_2(1,j_2)/(C_2(1,j_2)+x_2(j_2,i_2)));
    end
end

%To calculate the beta vector
r_2 = size(theta1_2);
beta1_2 = zeros(1,r_2(2));

```

```

beta2_2 = zeros(1,r_2(2));
h_2 = 1;
e_2 = 1;

for h_2 = 1:z_2(2)
    if h_2 <= r_2(2)
        beta1_2(1,h_2) = 90 - 180/pi*(atan(x_2(h_2,51)));
    else if h_2 == r_2(2)+1
        beta_max_2;
    else if h_2 >= r_2(2)+2
        beta2_2(1,e_2) = 180/pi*(atan(1/(0.5*(-
(C_2(1,h_2)+x_2(h_2,51))+sqrt((C_2(1,h_2)+x_2(h_2,51))*(C_2
(1,h_2)-3*x_2(h_2,51))+4*A_2)))));
        e_2 = e_2+1;
    end
end
end
end

beta_2 = horzcat(beta1_2,beta_max_2,beta2_2);

%Offset
thetaos_2 = theta_2+d_os;
thetaos_2_n = (thetaos_2*-1)+2*d_os;

%To calc the Mn vector, pressure, temp, and density ratios,
Mach 2 vector,
%and the del(s)/R vector
Mn_2 = M1_2*sin(pi/180*(beta_2));
p2p1_2 = (2*g*Mn_2.^2-(g-1))/(g+1);
p2p1os_2 = p2p1_2*p_os;
r2r1_2 = (g+1)*Mn_2.^2./(2+(g-1)*Mn_2.^2);
r2r1os_2 = r2r1_2.*r_os;
T2T1_2 = p2p1os_2./r2r1os_2;
dsR_2 = g/(g-1)*log(T2T1_2)-log(p2p1os_2);
Mn2_2 = sqrt((1+0.5*(g-1)*Mn_2.^2)./(g*Mn_2.^2-0.5*(g-
1)));
M2os_2 = Mn2_2./sin(pi/180*(beta_2-thetaos_2));

%For Sonic Point
sonictheta = beta_2 - asind(Mn2_2);
p=1;
for p=1:size(thetaos_2,2)
    if abs(sonictheta(p)-thetaos_2(p)) < 1e-
1*(min(abs(sonictheta(p)),abs(thetaos_2(p))))
        sonicpoint = thetaos_2(p);
    end
end

```

```

        sonic_pressure = p2plos_2(p);
    end
end

figure(1)
plot(theta, p2p1, 'b', thetaos_2, p2plos_2, 'r', theta_n,
p2p1, 'b', thetaos_2_n, p2plos_2,
'r',sonicpoint,sonic_pressure,'*k',sonicpoint*-
1+2*d_os,sonic_pressure,'*k')
xlabel('Deflection Angle, Theta, in degrees')
ylabel('Pressure Ratio, P_2/P_1')
string = sprintf('Shock Polar Plot with Offset = %0.2f,
Incident Mach Number = %0.2f',d_os,M1);
string2 = sprintf('Reflected Mach Number = %0.2f, and Gamma
= %0.2f',M1_2,g);
title({string,string2})
legend('Blue = Incident SW', 'Red = Reflected
SW','location','southwest')
grid on

col_header = {'Theta' 'Beta' 'Mn' 'P2/P1' 'r2/r1' 'T2/T1'
'del(s)/R' 'M2'};

if Table == 1
    xlswrite('PolarPlot.xlsx',col_header,'Incident Shock
Wave','A1')
    xlswrite('PolarPlot.xlsx',theta,'Incident Shock
Wave','A2')
    xlswrite('PolarPlot.xlsx',beta,'Incident Shock
Wave','B2')
    xlswrite('PolarPlot.xlsx',Mn,'Incident Shock
Wave','C2')
    xlswrite('PolarPlot.xlsx',p2p1,'Incident Shock
Wave','D2')
    xlswrite('PolarPlot.xlsx',r2r1,'Incident Shock
Wave','E2')
    xlswrite('PolarPlot.xlsx',T2T1,'Incident Shock
Wave','F2')
    xlswrite('PolarPlot.xlsx',dsR,'Incident Shock
Wave','G2')
    xlswrite('PolarPlot.xlsx',M2,'Incident Shock
Wave','H2')
    xlswrite('PolarPlot.xlsx',col_header,'Reflected Shock
Wave','A1')
    xlswrite('PolarPlot.xlsx',thetaos_2,'Reflected Shock
Wave','A2')

```

```

        xlswrite('PolarPlot.xlsx',beta_2,'Reflected Shock
Wave','B2')
        xlswrite('PolarPlot.xlsx',Mn_2,'Reflected Shock
Wave','C2')
        xlswrite('PolarPlot.xlsx',p2p1os_2,'Reflected Shock
Wave','D2')
        xlswrite('PolarPlot.xlsx',r2r1os_2,'Reflected Shock
Wave','E2')
        xlswrite('PolarPlot.xlsx',T2T1_2,'Reflected Shock
Wave','F2')
        xlswrite('PolarPlot.xlsx',dsR_2,'Reflected Shock
Wave','G2')
        xlswrite('PolarPlot.xlsx',M2os_2,'Reflected Shock
Wave','H2')
end

```


Appendix C: CEA Output

NASA-GLENN CHEMICAL EQUILIBRIUM PROGRAM CEA2, FEBRUARY 5,
2004

BY BONNIE MCBRIDE AND SANFORD GORDON

REFS: NASA RP-1311, PART I, 1994 AND NASA RP-1311,
PART II, 1996

```
prob case=11156976 det
p,atm  2.40 2.52
t,k    392.5 399.8
o/f    7 4
output short
output trace=1e-5
reac
fuel  H2  wt%= 100.
oxid  O2  wt%= 100.
end
```

DETONATION PROPERTIES OF AN IDEAL REACTING GAS
CASE = 11156976

ENERGY	REACTANT TEMP	WT FRACTION
		(SEE NOTE)
KJ/KG-MOL	K	
FUEL	H2	1.0000000
0.000	0.000	
OXIDANT	O2	1.0000000
0.000	0.000	

O/F= 7.00000 %FUEL= 12.500000 R,EQ.RATIO= 1.133812
PHI,EQ.RATIO= 1.133812

UNBURNED GAS

P1, BAR	2.4318	2.5534	2.4318	2.5534
T1, K	392.50	392.50	399.80	399.80
H1, KJ/KG	246.54	246.54	265.75	265.75
M1, (1/n)	11.192	11.192	11.192	11.192
GAMMA1	1.3935	1.3935	1.3930	1.3930
SON VEL1,M/SEC	637.4	637.4	643.2	643.2

BURNED GAS

P, BAR	35.453	37.289	34.781	36.583
T, K	3801.40	3811.01	3798.74	3808.35
RHO, KG/CU M	1.5194 0	1.5953 0	1.4908 0	1.5652 0
H, KJ/KG	3312.96	3318.62	3326.34	3332.01
U, KJ/KG	979.63	981.20	993.21	994.79
G, KJ/KG	-65707.6	-65764.0	-65704.0	-65760.6
S, KJ/(KG) (K)	18.1566	18.1271	18.1719	18.1424
M, (1/n)	13.546	13.556	13.537	13.548
(dLV/dLP)t	-1.07720	-1.07685	-1.07745	-1.07710
(dLV/dLT)p	2.2385	2.2301	2.2433	2.2348
Cp, KJ/(KG) (K)	15.7939	15.6748	15.8551	15.7355
GAMMAS	1.1332	1.1335	1.1331	1.1334
SON VEL,M/SEC	1626.1	1627.7	1626.0	1627.6

DETONATION PARAMETERS

P/P1	14.579	14.604	14.303	14.327
T/T1	9.685	9.710	9.502	9.526
M/M1	1.2103	1.2113	1.2096	1.2105
RHO/RHO1	1.8219	1.8218	1.8208	1.8207
DET MACH NUMBER	4.6476	4.6520	4.6026	4.6070
DET VEL,M/SEC	2962.6	2965.4	2960.6	2963.4

MOLE FRACTIONS

*H	8.3959-2	8.3367-2	8.4362-2	8.3769-2
HO2	1.6808-4	1.7160-4	1.6702-4	1.7053-4
*H2	2.0293-1	2.0282-1	2.0307-1	2.0296-1
H2O	5.3210-1	5.3317-1	5.3117-1	5.3224-1
H2O2	2.3919-5	2.4741-5	2.3627-5	2.4441-5
*O	2.7661-2	2.7460-2	2.7812-2	2.7612-2
*OH	1.2564-1	1.2561-1	1.2580-1	1.2577-1
*O2	2.7512-2	2.7373-2	2.7599-2	2.7460-2

* THERMODYNAMIC PROPERTIES FITTED TO 20000.K

NOTE. WEIGHT FRACTION OF FUEL IN TOTAL FUELS AND OF
OXIDANT IN TOTAL OXIDANTS

DETONATION PROPERTIES OF AN IDEAL REACTING GAS
CASE = 11156976

	REACTANT	WT FRACTION
ENERGY	TEMP	
		(SEE NOTE)
KJ/KG-MOL	K	
FUEL	H2	1.0000000
0.000	0.000	
OXIDANT	O2	1.0000000
0.000	0.000	

O/F= 4.00000 %FUEL= 20.000000 R,EQ.RATIO= 1.984171
 PHI,EQ.RATIO= 1.984171

UNBURNED GAS

P1, BAR	2.4318	2.5534	2.4318	2.5534
T1, K	392.50	392.50	399.80	399.80
H1, KJ/KG	341.95	341.95	368.57	368.57
M1, (1/n)	8.051	8.051	8.051	8.051
GAMMA1	1.3952	1.3952	1.3948	1.3948
SON VEL1,M/SEC	752.0	752.0	758.9	758.9

BURNED GAS

P, BAR	33.718	35.451	33.090	34.791
T, K	3542.48	3549.49	3541.56	3548.59
RHO, KG/CU M	1.0843 0	1.1384 0	1.0639 0	1.1170 0
H, KJ/KG	4392.16	4398.15	4412.11	4418.13
U, KJ/KG	1282.62	1284.14	1301.93	1303.46
G, KJ/KG	-79871.5	-79882.2	-79908.2	-79919.4
S, KJ/ (KG) (K)	23.7866	23.7443	23.8088	23.7665
M, (1/n)	9.472	9.477	9.468	9.473
(dLV/dLP)t	-1.03210	-1.03182	-1.03234	-1.03206
(dLV/dLT)p	1.5413	1.5356	1.5456	1.5398
Cp, KJ/ (KG) (K)	12.8862	12.7831	12.9547	12.8509
GAMMA _s	1.1491	1.1494	1.1489	1.1493
SON VEL,M/SEC	1890.2	1891.9	1890.3	1892.0

DETONATION PARAMETERS

P/P1	13.865	13.884	13.607	13.625
T/T1	9.025	9.043	8.858	8.876
M/M1	1.1766	1.1772	1.1760	1.1767
RHO/RHO1	1.8075	1.8073	1.8064	1.8063
DET MACH NUMBER	4.5432	4.5468	4.4996	4.5032
DET VEL,M/SEC	3416.6	3419.3	3414.7	3417.4

MOLE FRACTIONS

*H	7.5324-2	7.4640-2	7.5857-2	7.5171-2
HO2	1.0372-5	1.0482-5	1.0408-5	1.0519-5
*H2	4.5226-1	4.5267-1	4.5196-1	4.5237-1
H2O	4.3170-1	4.3223-1	4.3119-1	4.3171-1
*O	3.2606-3	3.2099-3	3.3059-3	3.2548-3
*OH	3.6247-2	3.6060-2	3.6466-2	3.6280-2
*O2	1.1945-3	1.1759-3	1.2104-3	1.1917-3

* THERMODYNAMIC PROPERTIES FITTED TO 20000.K

NOTE. WEIGHT FRACTION OF FUEL IN TOTAL FUELS AND OF
OXIDANT IN TOTAL OXIDANTS

Appendix D: Velocity Calculations

Placement	PDE Tube		Middle		Shock Wave			
	x	y	x	y	x	y	Tot. Length	Velocity m/s
0 ns								
Particle 1	111	142						
Particle 2	104	154						
20k ns								
Particle 1			148	146			18.6	930.4
Particle 2			142	158			19.1	955.2
40k ns								
Particle 1					188	155	20.5	1025.0
Particle 2					180	165	19.3	966.0
60k ns								
Particle 1					233	153	22.5	1126.1
Particle 2					222	171	21.2	1060.7
Particle 1 Series 2			148	131				
Particle 2 Series 2			137	143				
Particle 3 Series 2			130	154				
80k ns								
Particle 1 Series 2					185	131	18.5	925.0
Particle 2 Series 2					172	144	17.5	875.4
Particle 3 Series 2					167	160	18.7	937.1
100k ns								
Particle 1 Series 2					221	134	18.1	903.1
Particle 2 Series 2					210	148	19.1	955.2
Particle 3 Series 2					205	165	19.2	958.2
120k ns								
Particle 1 Series 2					263	134	21.0	1050.0
Particle 2 Series 2					248	150	19.0	951.3
Particle 3 Series 2					248	167	21.5	1076.2
Particle 1 Series 3	94	117						
Particle 2 Series 3	87	118						
Particle 3 Series 3	85	121						
140k ns								
Particle 1 Series 3			126	117			16.0	800.0

Particle 2 Series 3			120	118			16.5	825.0
Particle 3 Series 3			111	122			13.0	650.5
160k ns								
Particle 1 Series 3			161	119			17.5	876.4
Particle 2 Series 3			154	119			17.0	850.4
Particle 3 Series 3			142	124			15.5	776.6
180k ns								
Particle 1 Series 3					196	119	17.5	875.0
Particle 2 Series 3					190	120	18.0	900.3
Particle 3 Series 3					176	125	17.0	850.4
Particle 1 Series 4	100	124						
Particle 2 Series 4	81	128						
200k ns								
Particle 1 Series 4			139	127			19.6	977.9
Particle 2 Series 4	109	130					14.0	701.8
220k ns								
Particle 1 Series 4					183	128	22.0	1100.3
Particle 2 Series 4			140	131			15.5	775.4
240k ns								
Particle 1 Series 4					185	129	1.1	55.9
Particle 2 Series 4					170	133	15.0	751.7
Particle 1 Series 5	64	132						
260k ns								
Particle 1 Series 5	89	132					12.5	625.0
280k ns								
Particle 1 Series 5			115	134			13.0	651.9
300k ns								
Particle 1 Series 5					141	136	13.0	651.9
Particle 1 Series 6			105	117				
320k ns								
Particle 1 Series 5					174	135	16.5	825.4
Particle 1 Series 6			128	120			11.6	579.9
Particle 1 Series 7	98	108						
340k ns								
Particle 1 Series 6					152	119	12.0	600.5
Particle 1 Series 7			122	108			12.0	600.0

Particle 1 Series 8			113	150				
360k ns								
Particle 1 Series 7					146	108	12.0	600.0
Particle 1 Series 8			143	151			15.0	750.4
Particle 1 Series 9	97	87						
380k ns								
Particle 1 Series 8					172	151	14.5	725.0
Particle 1 Series 9			125	84			14.1	704.0